https://doi.org/10.1016/j.jmps.2021.104300

On the attraction power of critical state in granular materials

Na Deng[1], Antoine Wautier[2*], Yannick Thiery[3], Zhen-Yu Yin[4], Pierre-Yves Hicher[5], and François Nicot[1]

[1]*Grenoble Alpes University, INRAE, UR ETGR, 2 rue de la Papeterie-BP 76, 38402 St-Martin-d'Hères, France*

[2]*INRAE, Aix-Marseille University, UR RECOVER, 3275 Rte Cézanne, CS 40061, 13182 Aix-en-ProvenceCedex 5, France*

[3]*BRGM (French Geological Survey), Risk and Prevention Division, Orléans, France*

[4]*Department of Civil and Environmental Engineering, The Hong Kong Polytechnic University, Hong Kong, China*

[5]*Research Institute in Civil Engineering and Mechanics (GeM), UMR CNRS 6183, Ecole Centrale de Nantes, Nantes, France*

Abstract

The aim of this paper is to offer a fresh perspective on the classic concept of critical state (CS) in granular materials by suggesting that CS can be

*Corresponding author
Email address: antoine.wautier@inrae.fr (Antoine WAUTIER)

defined through the use of a single proportional strain test. In classic conventional testing, CS manifests itself under constant lateral stress and controlled strain in one given direction whenever continuous shearing is applied without change being induced to material volume. However, a comparison between proportional strain tests and biaxial tests simulated with DEM has clearly shown that the CS line (CSL) characterized by stresses, void ratio and fabric indexes can act as an attractor. The mechanical responses and fabric metrics evolve along dilatant proportional strain loading paths according to similar values after the strain level has become large enough to wipe out the material memory in the homogeneous domains considered in this analysis, i.e., the shear band area in dense samples and the whole area in loose samples. This suggests that the micro-structure of a granular material subjected to any dilatant proportional strain loading paths evolves while preserving its ability to withstand shearing without volume change at any time. Therefore, the CS concept can be generalized to a wide class of loading paths which shows that CS acts as a general attractor irrespective of the loading path considered.

Keywords: Critical state; Shear band localization; Homogeneous domain; Proportional strain loading path; Biaxial loading path; Granular materials; DEM simulation

1 Introduction

Although the structure of a granular material appears to be simple at the microscopic scale, its behavior shows itself to be complex at the macroscopic scale, mostly due to

the collective rearrangement of particles. Based on the gain or loss of contacts, granular materials will easily adjust to any change under loading conditions. Among the accessible micro-structures, some have the ability to withstand constant shearing with no change of volume. A state with such micro-structures is known as critical state (CS) and plays a leading role in the most popular constitutive relations for granular materials. The concept of critical state was first proposed by Casagrande [3] and developed by Roscoe et al. and Schofield et al. [34, 37] in the form of a stationary state where stress and volume tend to be constant under continuous shear strain. A steady stress ratio and a steady void ratio are two conditions for this classical definition of critical state [41].

The CS concept is the basic principle behind critical state soil models [1, 2, 21] and its importance in constitutive model cannot be underestimated, which explains its persistence as a concept. Enormous efforts have been devoted to verifying the conjecture of the uniqueness of the Critical State Line (CSL) [12, 47, 35] and to constructing appropriate mathematical descriptions of CS to improve the capability of constitutive models [20, 23] to simulate the mechanical behavior of granular materials. The evolution of internal soil structures along physical tests have been analyzed for enriching constitutive models based on micro mechanical investigations [19, 47, 14]. With the development of numerical tools, such as the Discrete Element Method (DEM) [5], it has been possible to describe more precisely micro-structures at critical state based on microscopic and mesoscopic descriptions [11, 12, 17, 13, 18, 48, 16]. It has been observed that microscopic or mesoscopic quantities such as metrics about fabric tensor and loop population also remain constant at critical state [12, 48]. It can be shown that the difference between the actual porosity and the CS porosity does not in itself determine the evolution of the micro-structure. The coaxiality between the plastic strain rate direction and the fabric anisotropy proved

to be a relevant state variable in defining critical state [22, 41]. A third condition that quantifies the role of fabric anisotropy in terms of its intensity and its relative orientation with respect to loading direction should also be taken into account, in addition to the aforementioned two conditions of constant stress ratio and void ratio [22, 41].

Research on CS is nearly exclusively based on conventional tests (triaxial tests in 3D or biaxial tests in 2D) in which a constant lateral stress condition $\mathrm{d}\sigma_{\mathrm{lateral}} = 0$ is imposed together with a constant strain rate in one given direction $\mathrm{d}\varepsilon_{\mathrm{axial}} = \text{constant}$ [1, 2, 12, 13, 48]. This preferential selection is linked to the tendency of generating constitutive models to work with stress and to calculate the resulting strains, as well as the difficulty of imposing fully controlled strain paths in the laboratory [15, 8]. For conventional loading, the $p - q$ path is preset; samples are loaded by increasing the axial incremental strain under constant lateral confining pressure; volumetric strain and deviatoric stress responses are recorded according to the loading path. This test allows for the existence of stationary states in volume and stress (the so-called critical state). Proportional strain tests, on the other hand, have been much less studied whereby the loading is imposed by proportional strain rates in the axial and lateral directions with $\mathrm{d}\varepsilon_{\mathrm{lateral}} = \lambda \mathrm{d}\varepsilon_{\mathrm{axial}}$ and $\mathrm{d}\varepsilon_{\mathrm{axial}} = \text{constant}$. Under proportional strain loading condition, the volumetric strain is no longer a response but a loading variable and the stress path is not known beforehand, which makes the interpretation of such tests more complex than it is for triaxial or biaxial tests. Except for the particular case of the undrained triaxial test, whereby the volume is kept constant, the continuous change in volume prevents stationary states in volume and stress along proportional strain paths to be observed. Without the existence of a stationary state, investigating the evolution of the micro-structures along a proportional strain loading path becomes a major challenge. In other words, tracking

the relation between triaxial (or biaxial) and proportional strain loading paths in terms of mechanical responses and underlying micro-structures is an open and stimulating topic.

In order to generalize the concept of CS, we focus on the relation between the material responses under dilatant proportional strain loading paths and biaxial loading paths in 2D. These two types of loading paths, as well as mixed biaxial/proportional strain paths, have been simulated by DEM. The details of the DEM simulation are shown in Section 2. Mechanical responses along biaxial tests and proportional strain paths are presented in Section 3. The relation between proportional strain tests and biaxial tests in the $p-q-e$ space is analysed in Section 4. In Section 5, the fabric-related CS locus is studied. The mechanical responses along the mixed loading paths are presented in Section 6, as is the relation between the imposed dilatancy in proportional strain tests and the dilatancy in biaxial tests.

2 DEM simulation

The Discrete Element Method (DEM) [5] is a powerful numerical method to simulate the global behavior of a set of grains interacting through contact laws. It has been widely used to simulate the mechanical response of granular assemblies under various loading conditions. The mechanical states are characterized locally by kinematic information including position, rotation and velocity of grains, as well as static information based on contact force between contacting particles. In this study, the open source software YADE [40] has been used.

Under consideration here is a quasi-2D soil sample in the form of an assembly of a single layer of 20,000 spherical particles contained within a surface domain of 1 m $\times$ 1.5 m. The particle sizes have an average diameter $d_{50} = 0.008$ m and $d_{\max}/d_{\min} = 2$. The elasto-frictional law introduced by [5] has been adopted as the contact law. The cohesiveless contact parameters between two grains contain a normal and tangential linear spring of respective stiffness k_n and k_t, as well as a friction characterized by a friction angle $\phi = 35°$. k_n/D_s is given as 300 MPa, where $D_s = 2R_1R_2/(R_1 + R_2)$ and R_1, R_2 are the radii of particles in a given contact and k_t/k_n is 0.5. If the pressure of 100 kPa is considered, the average ratio of contact overlap and particle size $< u_n > /d_{50}$ is around 0.16%, which is close to the value (10^{-3}) in literature [18, 41]. For sample preparation, two schemes can be used to obtain an isotropic compression of the specimen: the boundary moving scheme and the internal compacting scheme [45]. In this study, particles are enlarged, at first, while keeping the boundary walls fixed to generate a preliminary sample up to 90 kPa. Then, to achieve a more precise consolidation pressure, the sample undergoes an isotropic consolidation by imposing an equivalent incremental strain on the boundaries in the vertical and lateral directions up to a specific consolidation state. During this preparation process, contact friction angles of 2° and 35° are used to obtain dense and loose samples, respectively. Consolidation pressures of 10 kPa, 20 kPa, 40 kPa, 60 kPa and 100 kPa are considered. Three dense samples and five loose samples are thus prepared and named as indicated in Table 1. The void ratio is accounted for, based on solid and void surfaces on the 2D plane as shown in Fig.1. During the shearing process, a contact friction angle $\phi = 35°$ is adopted in all the samples. Note that the soil mechanics convention is adopted throughout the paper with compression and contraction counted positive. As a result, dilatant/contracting volumetric strain are considered as negative/positive respectively.

For proportional strain tests, the **100kPa-dense** sample is used with an initial void ratio of 0.191. In the 2D simulation, $\mathrm{d}\varepsilon_1 = \lambda \mathrm{d}\varepsilon_2$ and $\mathrm{d}\varepsilon_2 = 10^{-2}\ \mathrm{s}^{-1}$. As $\mathrm{d}\varepsilon_v = (\lambda+1)\mathrm{d}\varepsilon_2$, $\lambda > -1$ corresponds to a contracting test, $\lambda = -1$ to a constant volume test, and $\lambda < -1$ to a dilatant test. We have adopted $\lambda = -1.2, -1.3, -1.4$ for the three dilatant proportional strain tests. Biaxial loading paths with corresponding pressures are applied to all the samples indicated in Table 1. The stress and strain states are then described in 2D as follows: deviatoric stress $q = \sigma_2 - \sigma_1$, mean stress $p = (\sigma_1 + \sigma_2)/2$, and volumetric strain $\varepsilon_v = \varepsilon_1 + \varepsilon_2$, where σ_1 and σ_2 are the principal stresses at horizontal and vertical directions and ε_1 and ε_2 are the principal strains. The direction 2 is always the vertical loading control direction ($\dot{\varepsilon}_2 = 10^{-2}\ \mathrm{s}^{-1}$), as shown in Fig.1. When the pressure ranges from 20 kPa to 200 kPa, the Inertial Number I of the granular system ranges among $2.77\mathrm{e}10^{-5}$ - $8.76\mathrm{e}10^{-5}$, which corresponds to a quasi-static state [6].

In reality a 2D model of a granular material is quantitatively different from sand assemblies; for example void ratio values and coordination numbers in 2D assemblies are smaller than those in 3D [12], and stresses express in kPa relies on the use of an arbitrary out of plane dimension [i]. However, given that the complexity of the constitutive behaviour of granular assemblies stems mainly from the local properties and the disordered packing, both effects can be captured in 2D simulations [30]. Qualitative investigations of granular materials based on DEM simulations in 2D can then be considered as both effective and efficient. Proof of such effectiveness and efficiency can be found in various studies of the microscopic mechanism behind the mechanical responses of granular materials under different loading paths have been investigated [12, 17, 13, 48, 25]. Thus, the 2D

[i] In the present study, the out of plane dimension is then taken equal to the thickness of the sample box (0.04 m), which allows kPa rather than kN/m to be used for the stress unit on the boundary walls. The thickness of the box has a proportional influence on the stress values, which should not impact the following results, at least qualitatively.

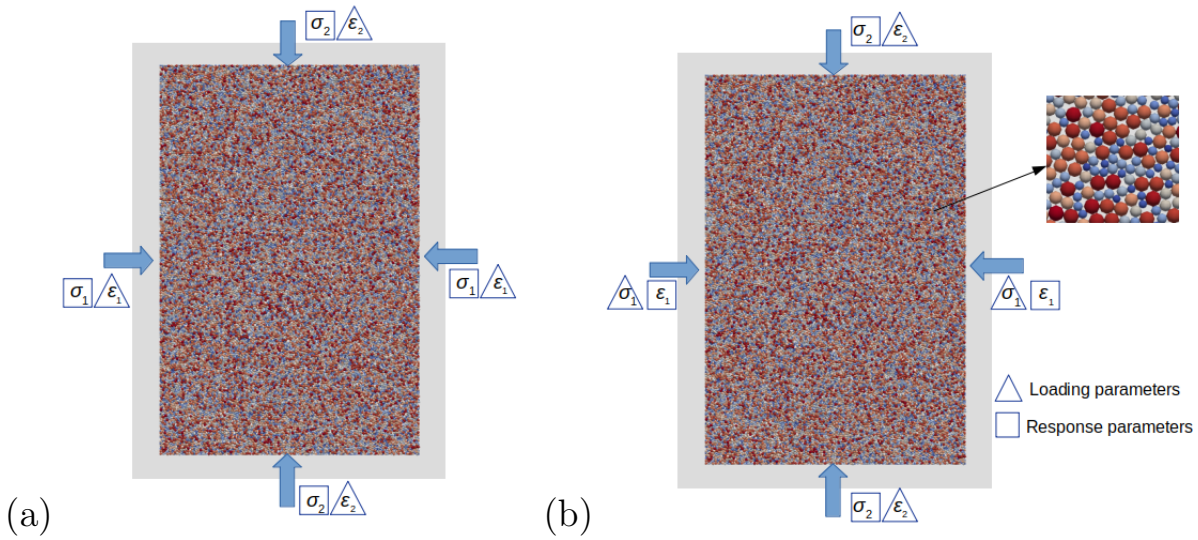

Figure 1: Quasi-2D DEM specimens for (a) proportional strain tests where loading parameters are ε_1 and ε_2 and (b) biaxial tests where loading parameters are ε_2 and σ_2. The direction 2 is always the vertical loading control direction at the REV scale.

assembly simulation is adequate enough for qualitative investigations of critical states under proportional strain and biaxial loadings performed in this study.

Table 1: Initial void ratios e_0 of prepared samples. The sample '**100kPa-dense**' is used in proportional strain tests)

Sample	40kPa-dense	60kPa-dense	**100kPa-dense**	10kPa-loose
e_0	0.197	0.195	**0.191**	0.266
Sample	40kPa-loose	60kPa-loose	100kPa-loose	20kPa-loose
e_0	0.267	0.265	0.261	0.267

3 Mechanical response

3.1 Mechanical response along dilatant proportional strain loading paths

3.1.1 Stress-strain analysis

Figure 2 shows the evolution of the deviatoric stress q along the axial strain ε_2 under dilatant proportional strain loading path with $\lambda = -1.2, -1.3, -1.4$. In this figure, it can be observed that the deviatoric stress q grows quickly at first and then decreases after the peak. Gradually, q decreases to 0. When $\lambda = -1.4$, the sample undergoes the fastest dilatancy and the corresponding stress curve reaches the earliest peak at $\varepsilon_2 = 0.013$ and the earliest zero deviatoric stress at $\varepsilon_2 = 0.061$. When $\lambda = -1.3$ and $\lambda = -1.2$, it appears that the peaks are reached at $\varepsilon_2 = 0.017$ and $\varepsilon_2 = 0.019$ because of smoother and smoother dilatancy. Zero mean pressure p occurs at $\varepsilon_2 = 0.085$ and $\varepsilon_2 = 0.142$, respectively.

3.1.2 Kinematic pattern: from localization to diffuse

The existence of a stress peak (Fig.2) corresponds to a generalized limit state [29] which has been shown to be a proper failure state [43]. Various failure modes, characterized by localized or diffuse patterns, can be encountered after the peak, along the descending branch. In biaxial tests, either diffuse or localized modes will appear [29]. In this study, however, these two modes appear successively along each proportional strain test. In this subsection, the incremental deviatoric strain distribution has been used to characterize the kinematic pattern, as introduced in literature [33, 48]. For example, in the test with $\lambda = -1.2$, a typical diagonal shear band traversing the whole specimen appears at $\varepsilon_2 = 0.008$, as shown in Fig.3 (I), corresponding to the point I in Fig.2. After a process

of dilatancy, the shear band begins to vanish in the strain state $\varepsilon_2 = 0.110$ shown in Fig.3 (II). Fig.3 (III) demonstrates the kinematic pattern when $\varepsilon_2 = 0.142$, where the mean pressure p is close to zero. An evolution from localization, when the strain largely concentrates in a partial domain of the material, to liquefaction, when the effective stress within the granular specimen is reduced to essentially zero, has been observed along the three dilatant proportional strain paths, as shown in Fig.3. With the increase in volume along the loading path ($\lambda < -1$), the density of the sample gradually decreases and the kinematic pattern changes from localized to diffuse until a zero mean pressure p is reached.

Kinematic patterns characterize the nature of the failure mode, together with the spatial domain. It has been widely accepted that fabric-related measures should be taken either within the shear bands or within the full sample when the shear deformation is diffuse, since measures within nonhomogeneous domains have no constitutive meaning [10, 12, 13, 48, 35]. In this study, the index M_{ed} [24] has been adopted to define the shear band domain. M_{ed} refers to an absolute difference of incremental deviatoric strain inside and outside the shear band with a trial width divided by their sum. Regarded as an optimization problem, the shear band width has been obtained according to the maximum M_{ed} within a reasonable range of the trial shear band width. More details are available in [24]. In the following section, labels with * refer to measures within a homogeneous domain (shear band for dense specimen and whole sample for loose specimen). Taking the kinematic evolution as its base, the next section will examine the evolution of the stress and void ratio.

3.2 Mechanical response along biaxial loading paths

As recalled in the introduction, the critical state (CS) refers to a state where stresses, void ratios and fabrics tend to be steady at relatively large deformation when shear strain further increases [41]. Biaxial tests used as references have been simulated to define the critical state line which refers to a collection of critical states obtained at different confining pressures. Typical macroscopic responses in biaxial tests are illustrated in Fig.4, where deviatoric stress and volumetric strain evolve with respect to axial strain ε_2. Figures on the left hand show the results from the dense samples. In these three figures, the deviatoric stresses show an increase before a peak is reached, and a decrease followed by a steady regime with small fluctuations. The stress peaks rise gradually with the increase in confining pressure from 40 kPa to 100 kPa. The volumetric strain shows a small contractancy, at first, and transfers to dilatancy before a steady state is reached. On the other hand, for the loose specimens, q and ε_v continuously rise up to steady states, as shown on the right-hand panel of Fig.4. Localized and diffuse patterns have developed within the dense and loose samples, respectively.

As highlighted in Subsection 3.1.2, it is important to focus on the domain within the shear band when considering void ratio and fabric indexes in order to characterize material scale properties by considering only homogeneous domains. The same point holds for stresses even if the stress heterogeneity is never reported in strain localization problems. Do stress patterns exhibit significant differences inside and outside the shear band? Is the stress path within the shear band the same as in the whole sample? Usually, stresses are obtained macroscopically from the external forces applied on the sample boundaries. To obtain the stresses within shear band, we have adopted a local definition based on Love-Weber stress at the grain scale. The mean stress tensor $\bar{\sigma}_{ij}^{p}$ of each particle can be

computed based on the contact forces applied, thanks to the Gauss theorem [31, 26]. More details are available in aforementioned literature. The stress tensor for a given domain Ω can be computed based on all N_p particles in the domain as $\sigma^*_{ij} = \frac{1}{\Omega}\sum_{p=1}^{N_\mathrm{p}} \bar{\sigma}^p_{ij} V^p$.

In Figure 5, global stress components have been compared with local stresses computed within the shear band domain for the 100kPa-dense sample under a biaxial loading path. Stresses based on boundaries, including principal stresses σ_1 and σ_2 in the whole sample, are compared with σ^*_1 and σ^*_2 considering the domain of the shear band based on the grain scale stress definition. In addition, the relative orientation of the stress tensor characterized by $(\theta_{\sigma^*_1} - \theta_{\sigma_1})$ is presented. It is observed that the evolution of stresses within the shear band and the whole sample is far more similar than it is for the void ratio [48] in 2D. Thus, it is reasonable to adopt stresses based on sample boundaries instead of stresses within the shear band when investigating critical state. This approach has been adopted throughout the rest of this paper. A precise characterization of the loading path within the shear band and its difference from the whole specimen is an issue that remains to be examined. At the moment, it is beyond the scope of this paper. Some preliminary results on stress rotation within shear bands can be found in Liu et al. [25] and more investigations and discussions on this issue will be conducted in further studies.

4 $p - q - e$ space analysis

The CSL is characterized by mean stress p, deviatoric stress q and void ratio e, usually plotted separately in planes (p, q) and (p, e). So, here, mechanical responses (p, q, e) from proportional strain tests and biaxial tests have been compared in $p - q$ and $p - e$ planes.

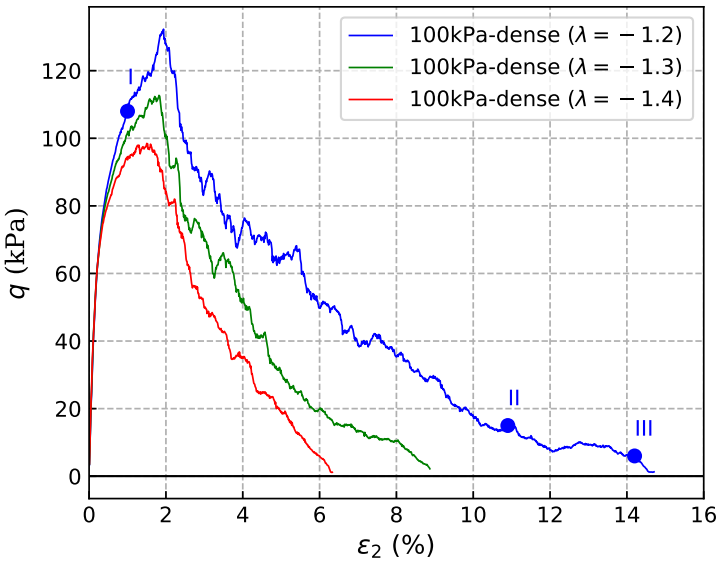

Figure 2: Evolution of the deviatoric stress q along dilatant proportional strain tests with different magnitudes of dilatancy characterized by $\lambda = -1.2, -1.3, -1.4$. Point I, point II and point III refer to onset of a well marked shear band at $\varepsilon_2 = 0.010$, slightly blurred shear band at $\varepsilon_2 = 0.109$, and the pressure p close to zero at $\varepsilon_2 = 0.142$, respectively. The corresponding kinematic patterns of these three points are shown in Fig.3

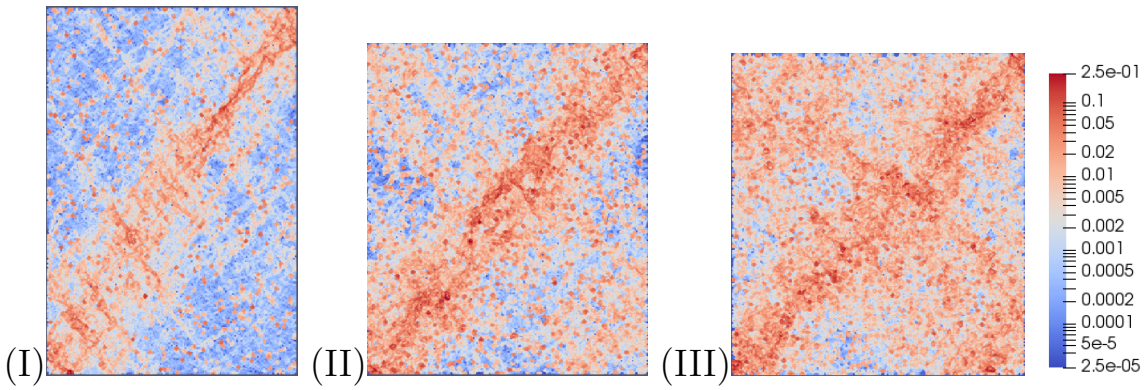

Figure 3: Incremental deviatoric strain maps ($\mathrm{d}\varepsilon_d$) estimated for axial strain increments of 0.11%. Three axial strains are considered along the proportional strain path $\lambda = -1.2$: (I) onset of a well marked shear band at $\varepsilon_2 = 0.010$, (II) slightly blurred shear band at $\varepsilon_2 = 0.109$, (III) just before liquefaction (p is close to 0) at $\varepsilon_2 = 0.142$. The corresponding points in $q - \varepsilon_2$ plane are shown in Fig.2

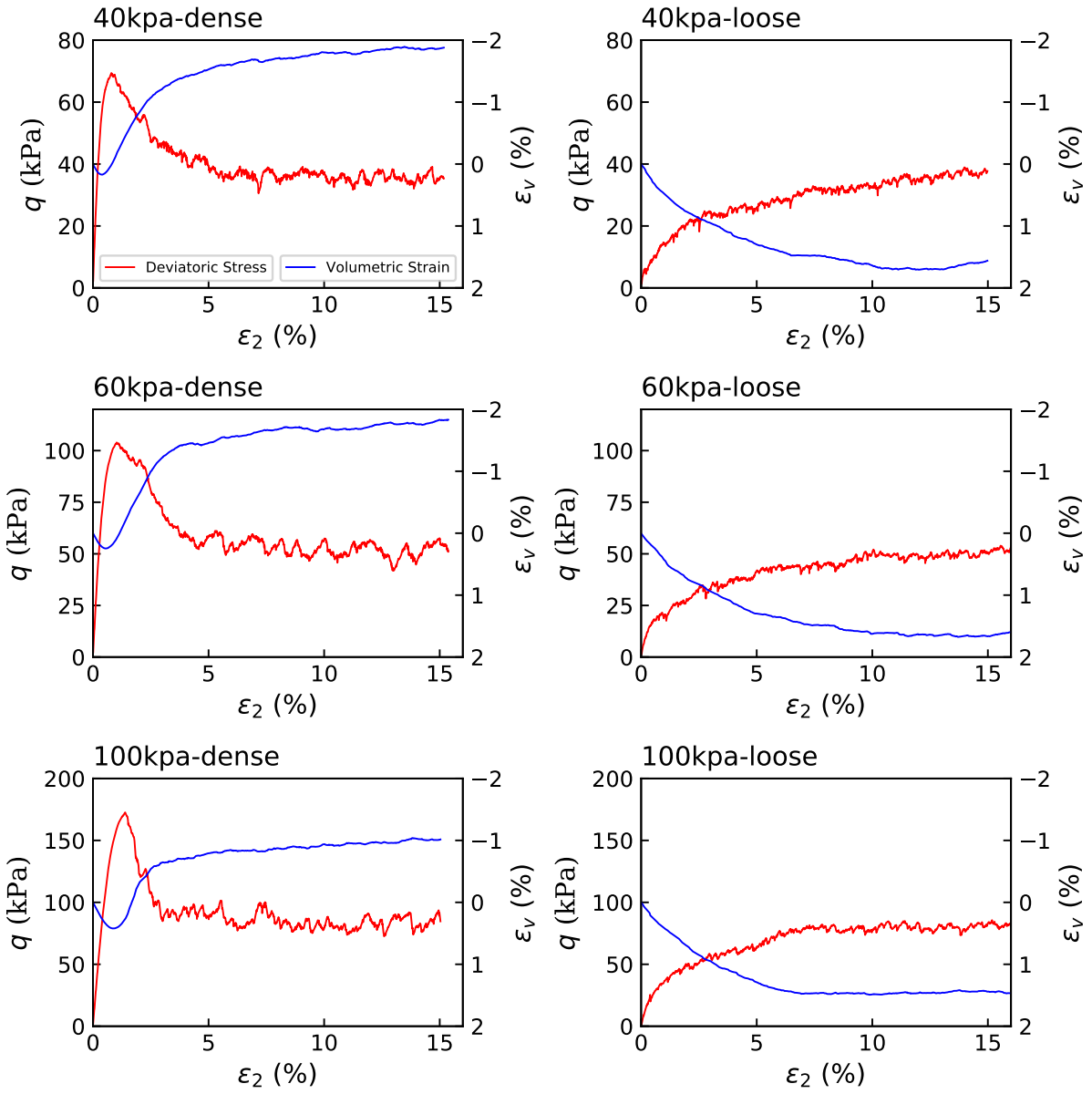

Figure 4: Deviatoric stress and volumetric strain of biaxial tests in dense (left panel) and loose (right panel) samples. Three biaxial loading paths with $\sigma_0 = 40$ kPa, 60 kPa and 100 kPa are considered. Note that soil mechanics convention is adopted with positive compression.

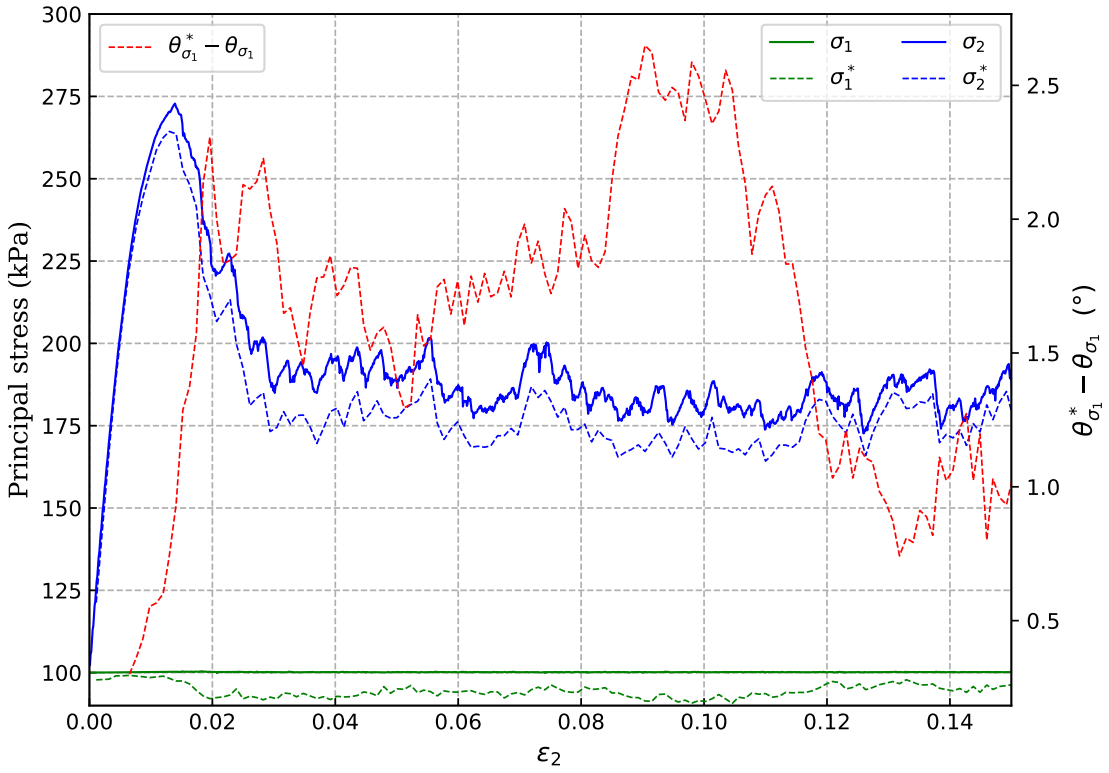

Figure 5: Principal stresses in the whole sample (σ_1 and σ_2) and within the shear band (σ_1^* and σ_2^*), and relative orientation of principal stress ($\theta^*_{\sigma_1} - \theta_{\sigma_1}$). The 100kPa-dense sample under biaxial loading path is adopted.

4.1 $p - q$ plane

Figure 6 illustrates the stress paths of the biaxial tests and the proportional strain tests. The three straight lines result from biaxial tests with dense samples. The initial states are marked with triangles and ultimate points are highlighted by squares labelled as A, B and C. The critical stress ratio line (CSRL) is given as a dashed line based on the three ultimate points, and the three highest points define the maximum stress ratio line (MSRL).

As for the dilatant proportional strain tests, Fig.6 shows that the path of the deviatoric stress and the mean stress (p, q) for each case, starts from the initial state of around (100 kPa, 0), evolves to the MSRL and, at the end, changes direction to turn back toward the zero-stress level along an asymptotic line after having formed a 'loop'. Result of a mixed biaxial test/proportional strain test is also presented in Fig.6. The sample was led to CS by a biaxial loading under 100kPa lateral stress upon which the loading mode was switched to a dilatant proportional strain loading. It can be seen that the stress path evolves from the very beginning along the CSRL with decreasing p and q.

Figure 5 illustrates that the stresses in the sample are relatively homogeneous at least in a 2D condition. The vanishing of the principal stresses along the dilatant proportional tests occurs simultaneously with the evolution from localized to diffuse failure (Figure 3). The vanishing of the principal stresses offers two possibilities: (1) liquefaction occurs only within the shear band and the behavior outside the shear band is regarded to be close to an elastic solid under unloading; (2) the kinematic pattern evolves gradually to become diffuse throughout the whole sample. In addition, it is worth noting that all computed results display an asymptotic behavior in the $p - q$ plane, approaching the CSRL independently of the imposed dilatancy ratio, as shown in Fig.6. This kind of stress track,

especially the loop, has scarcely been reported in the literature for dilatant proportional strain tests in either laboratory [15, 39, 7] or DEM simulations [32], with exception of the work reported by [4, 44, 8].

To further refine the classification of the stress response along proportional strain paths, a variety of proportional strain paths have been additionally simulated using specimens with different densities. The results are shown in Fig.7. Based on these results, the stress response path along proportional strain tests can be categorized into four types under different densities and volumetric strain rates, as illustrated in Fig.8. Group 1 results from one typical contracting strain path along which p and q increase continuously, and Group 2 comes from a typical dilatant proportional strain path leading to zero mean pressure p [7, 27]. Group 3 represents stress paths from a dense sample under proportional strain tests with a relatively small dilatant rate, whereas Group 4 demonstrates a stress path under a proportional strain test with a contracting rate in a dense sample, similar in trend to the stress path under an undrained loading.

It is worth paying attention to Group 3 because of the infrequently-reported 'stress loop'. A dense sample with imposed dilatancy was experimentally investigated by Ibraim et al. [15], Chu et al. [4] and Daouadji et al. [8], and numerically by Wan and Guo [44] and Nicot et al. [32]. The $p - q$ relation from [15] along such a loading path has been drawn in Fig.8. The stress path was stopped early with an axial strain of around 5%. If the test had been conducted further, with the growth of volume and a constant number of particles, an increasing number of contacts would probably have opened that would have resulted in a stress drop at some point. Indeed, the complete increase and decrease in q along such a loading path reported in [8] produced a stress path that was more like a back-

and-forth line than a loop. This may have been the case because it was a middle dense sample with a not very pronounced softening. Both the limited shearing strain and the use of the middle dense samples could explain why no such loops were observed, even for similar loading conditions [32]. Such loops were, however, reported in [44, 38]. The Group 3 type has also been obtained in 3D simulations not included in this paper which focuses on 2D simulations. It would be worth to conduct a detailed 3D investigation in the future.

As for the type of Group 4, stress softening was observed both along isochoric and contracting proportional strain loading paths. The slight decrease in the deviatoric stress q is linked to strain localization within the sample, since shear bands were generated in these two simulations. As underlined in [44], the slope of the stress path under a contractant proportional strain loading depends on the volumetric strain rate. But, according to the results in Fig.6, the critical stress ratio in proportional strain tests is independent of λ when the axial strain is large enough, as shown in Fig.6.

4.2 $p - e$ plane

Void ratios e^* within the shear band are tracked for dense samples, and global void ratios e^* for loose samples. The void ratio is given in 2D by $e^* = (A_{sb} - A_s)/A_s$, where A_{sb} and A_s denote, respectively, the total and solid areas of the shear band. The evolution of e^* is represented in Fig.9, with respect to mean stress p.

As for proportional strain tests shown in Fig.9 (a), the results converge to a master curve in the $p - e^*$ plane independent of the dilatant rate characterized by λ. When the starting point of the proportional strain loading is at critical state under a biaxial loading, the (p, e^*) curve will follow the master curve from the very beginning of the proportional

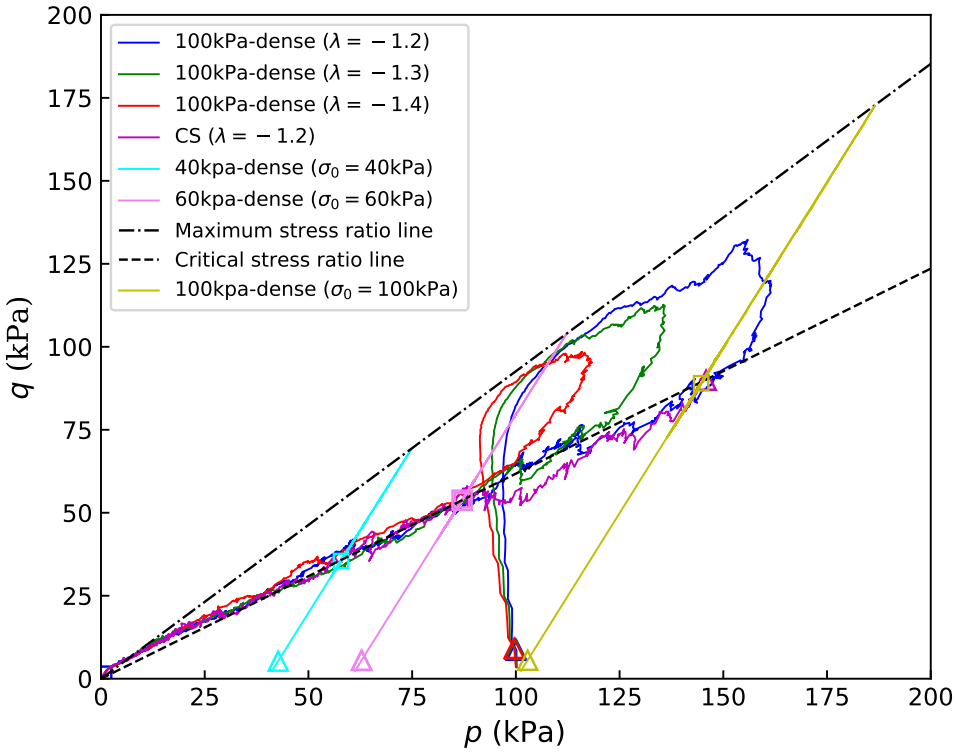

Figure 6: Stress paths of biaxial tests and proportional strain tests in $p - q$ plane. The start and end points are marked by triangles and squares, respectively. The critical stress ratio curve and the maximum stress ratio curve are drawn according to the critical states and the maximum value from biaxial tests, respectively.

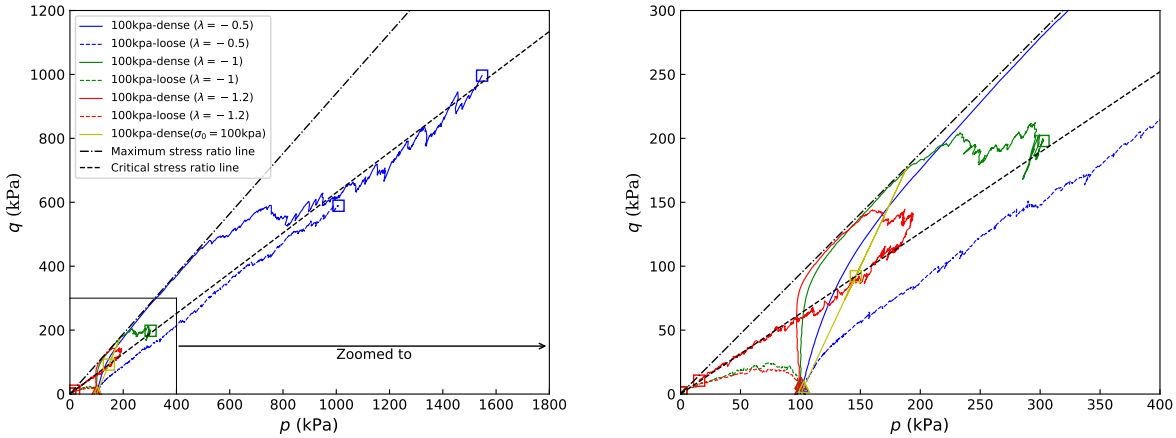

Figure 7: Stress paths in $p - q$ plane along six proportional strain tests and one biaxial test. Dilatant ($\lambda = -1.2$), undrained ($\lambda = -1$) and contracting ($\lambda = -0.5$) proportional strain paths are conducted with the samples labelled 100kPa-dense and 100kPa-loose. A biaxial loading path is performed in the sample 100kPa-dense. The square domain is zoomed up on the right hand side.

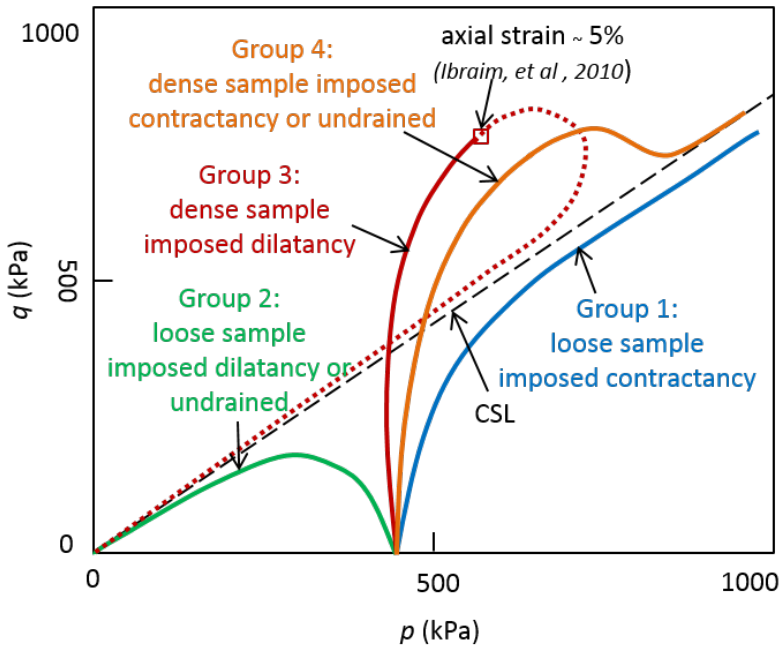

Figure 8: Four categories of stress path along proportional strain tests according to DEM simulation results shown in Fig.7.

strain loading.

As for biaxial tests with confining pressures of 40 kPa, 60 kPa and 100 kPa, the results illustrated in Fig.9 (b) are consistent with experimental observations in [10] and DEM simulations in [48]. Namely, e^* from dense samples, after dilatancy, evolves to meet e^* of loose samples at the critical state. For a more precise representation of the CSL in the (p, e^*) plane, two biaxial test results with confining pressures at 10 kPa and 20 kPa have been included.

These critical states with proportional strain tests in $p - e^*$ plane are compared. An interesting feature stands out: the fitting curve of $p - e^*$ from proportional strain tests crawls just along the critical state curve obtained from the biaxial tests. Even though the CS from nine biaxial tests can lead to the critical state line, the master curve obtained from fitting a curve to a cluster of $p - e^*$ data in dilatant proportional strain tests, com-

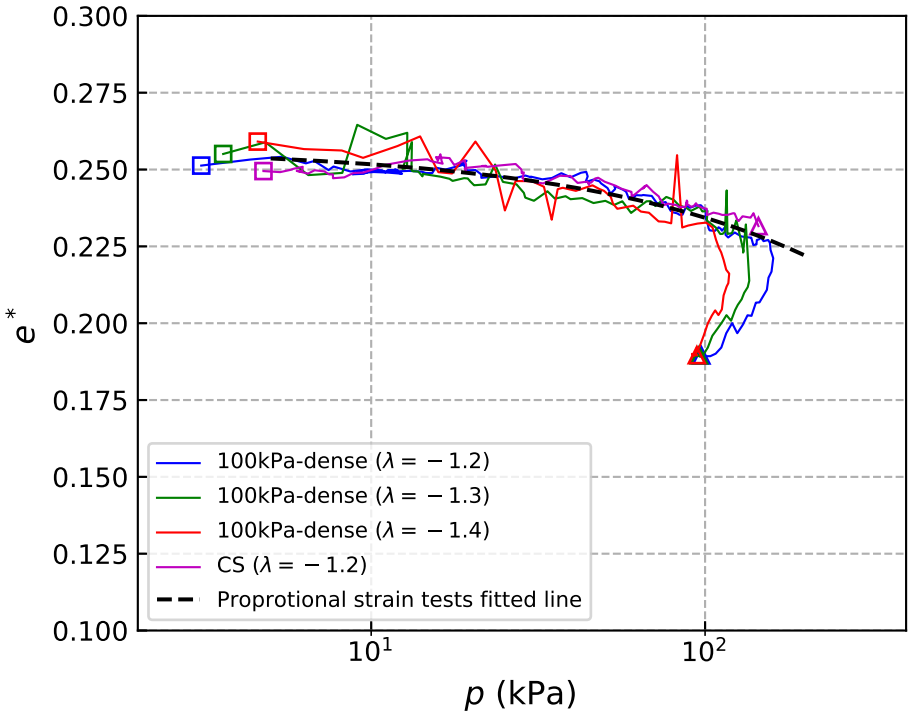

(a)

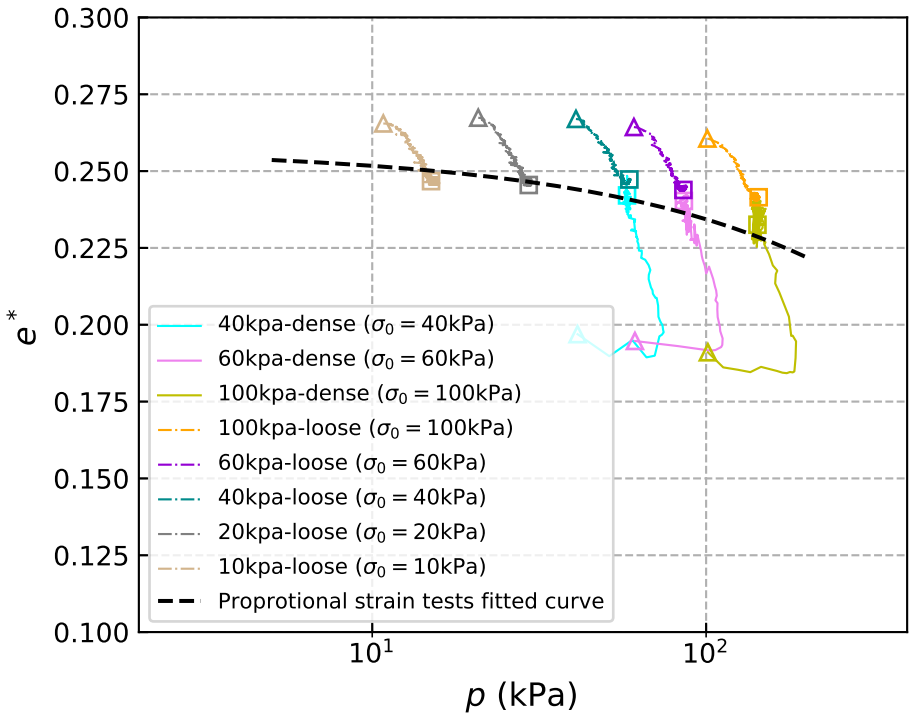

(b)

Figure 9: $p - e^*$ evolution in proportional strain (a) and biaxial (b) tests. The start and end points are marked by triangles and squares, respectively. A fit based on a power function is shown for proportional strain tests and repeated to compare with the results from biaxial tests, as all dilatant proportional strain tests converge towards a master curve. The equation of the fitted curve is $e^* = 0.2571 - 0.02275(\frac{p}{100})^{0.6274}$.

pared to the nine CS obtained from biaxial tests, induces less uncertainty.

It is worth noting that the fitting curve is based on a power function rather than a logarithmic function. It has been proved experimentally [42, 23] that, unlike in clay, the critical state line for granular materials cannot be estimated by a straight line in the $e - \log p$ plane. Thus, the commonly used CSL expression $e_c = \mathrm{A} + \mathrm{B}\ \ln p_c$ is generally not representative for granular materials, where the e_c and p_c are the critical void ratio and the critical pressure; A and B are two constants characterizing a given material. The relation of e_c and p_c for granular materials can be expressed as $e_c = \mathrm{D} - \mathrm{E}\ (\frac{p_c}{\mathrm{F}})^{\mathrm{G}}$, where F is a reference pressure, usually the atmospheric pressure (101 kPa) for convenience, and D, E, and G are dimensionless constants that can be identified from experiments on a given material [20, 46].

In summary, from Fig.6 and Fig.9, it can be observed that the master curves (p, q) and (p, e^*) from dilatant proportional strain tests agree well with the critical state lines from biaxial tests after a sufficiently large strain level has been imposed (or immediately if the initial state is already a critical state). Hence it is shown that the classical critical state surface defined in $p - q - e$ space for a given granular materials can be obtained by performing one single dilatant proportional strain test. To the best of our knowledge, no such results have been reported in the literature. For a further analysis of this relation, the following sections will investigate the micro/meso-structures of the samples under proportional strain and biaxial tests, as well as under mixed biaxial/proportional strain tests.

5 Fabric-related critical state locus

Even though the critical state is most often characterized by the relation between the mean stress p, the deviatoric stress q and the void ratio e when stress and strain rate directions are fixed [41], the evolution of the fabric is also an important feature to be added to the $p-q-e$ space in order to stay within the framework of Anisotropic Critical State Theory (ACST) that requires the values of the fabric to be steady.

5.1 Fabric tensor analysis

A fabric tensor quantifies micro-structural orientation-related characteristics of the material in a tensorial form [13]. In this subsection, the inter-particle contact normal directions are characterized by the second-order fabric tensor of $F_c = \frac{1}{Nc}\sum_{k=1}^{N_c} n^k \otimes n^k$, where N_c is the total number of inter-particle contacts in the assembly; n^k is the unit vector representing the normal direction of the kth contact. Only contacts in the shear band are considered. The norm of the normal at contact has to be normalized by the Lode angle in order to be unique in 3D. In the present 2D case there is no Lode angle; thus, no need for normalization. To make sure that the CS investigated within shear bands satisfies the third condition required by ACST as mentioned in Section 1, the orientation of the fabric tensor has been compared with the direction of the plastic flow which can be related to the stress tensor for monotonic radial loading [22]. The deviatoric orientation is less than 2.5 degrees throughout the whole biaxial test on the 100kPa-dense sample. The variable α_c^*, referring to the difference between the two principal components of F_c^* within the shear bands, is measured to characterize fabric anisotropy. $\alpha_c^* = 0$ refers to an isotropic fabric, whereas $\alpha_c^* = 1$ corresponds to the situation that the normal direction of all inter-particle

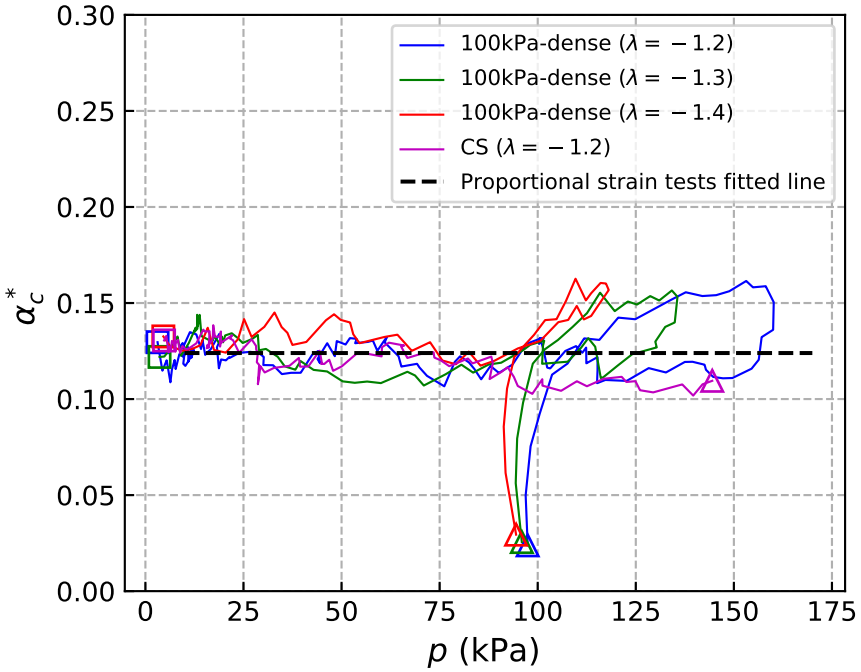

(a)

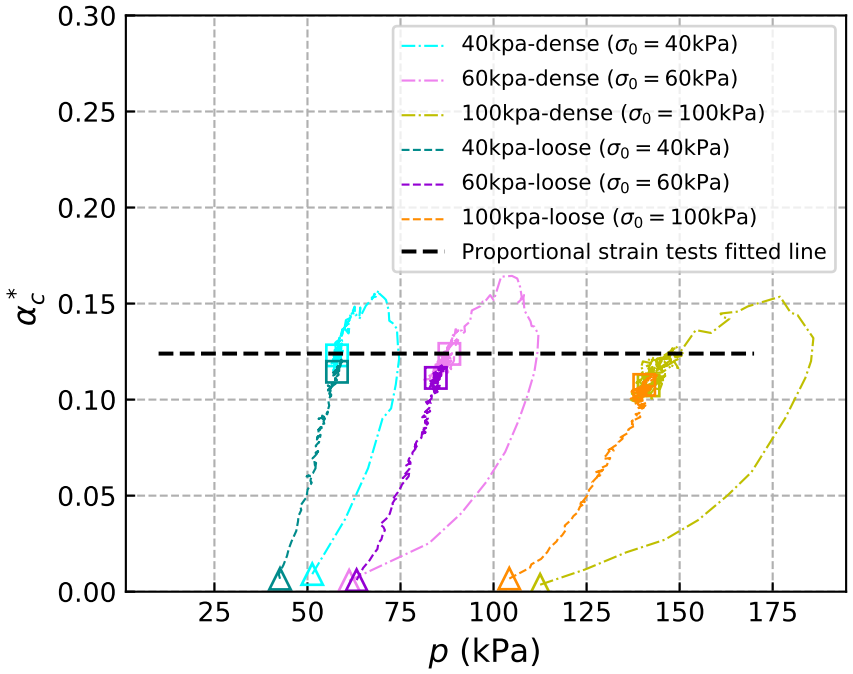

(b)

Figure 10: $p-\alpha_c^*$ evolution for proportional strain (a) and biaxial (b) tests. The start and end points are marked by triangles and squares, respectively. A linear fit is shown for the dilatant proportional strain tests and repeated on the biaxial tests, as all the proportional strain tests converge towards a master curve.

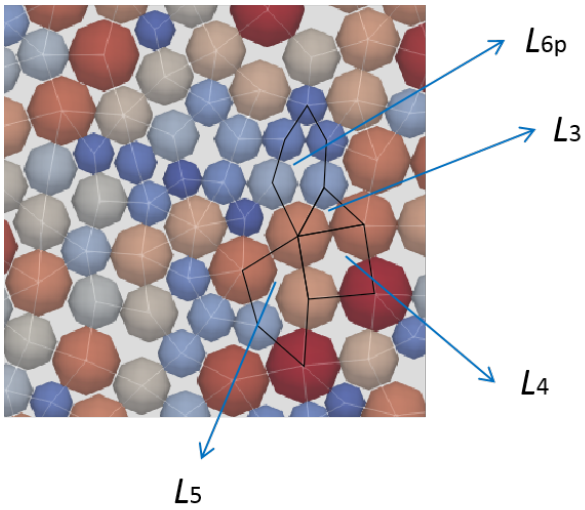

Figure 11: Meso-loop definition in granular materials

contacts investigated are exactly the same.

The evolution of α_c^* has been plotted in Fig.10 with respect to mean stress p. Except for the proportional strain loading starting from the CS, all the specimens have similar fabric characteristics in terms of variable α_c^* close to 0 at the initial states, due to the isotropic initial states where the inter-particle contact normal direction distribution is uniform in all the possible directions. As shown in Fig.10 (a), all $\alpha_c^* - p$ graphs from the proportional strain tests converge towards a master curve. A linear fit is given for the proportional strain tests and repeated in Fig.10 (b) to compare with the results from the biaxial tests. The relation between proportional strain tests and biaxial tests characterized by (p, q, e^*) has also been observed in the p-α^* plane, namely, the master curve obtained in proportional strain tests has gathered the critical states from biaxial tests. More importantly, all specimens under biaxial and proportional strain loading paths end up with the same anisotropy in the ultimate regime. The convergent feature at ultimate states along different loading paths is in line with the findings reported in the literature [12, 13].

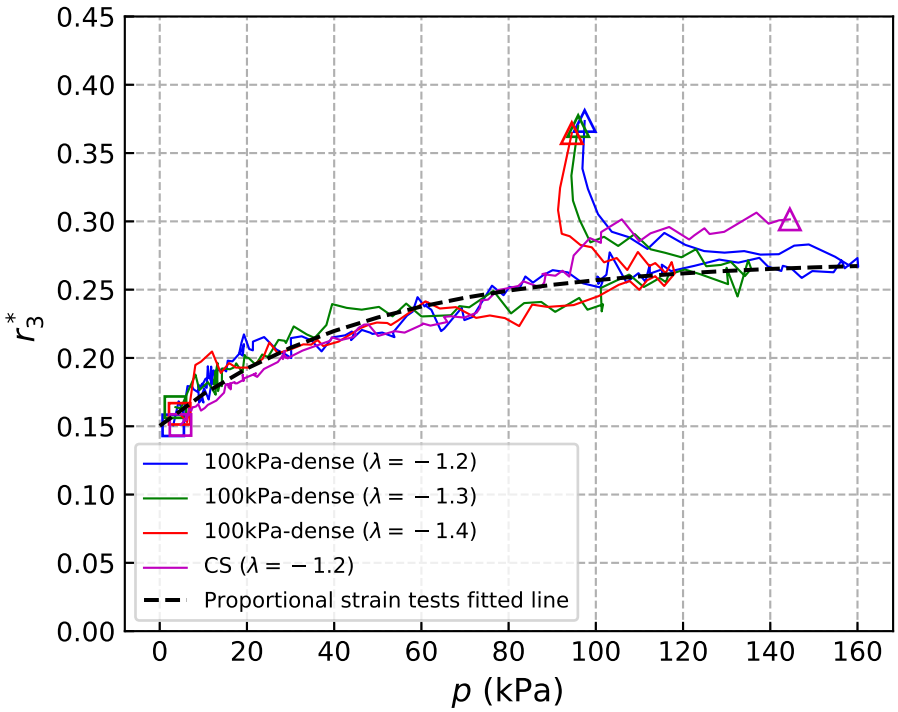

(a)

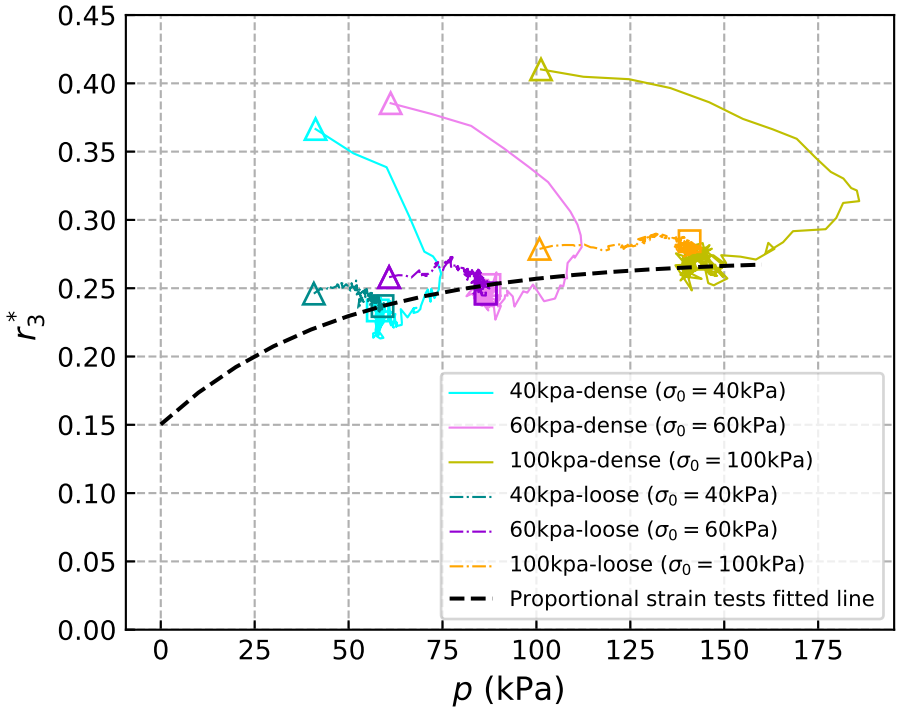

(b)

Figure 12: $p - r_3^*$ for proportional strain (a) and biaxial (b) test. The start and end points are marked by triangles and squares, respectively. An exponential fit is shown for the dilatant proportional strain tests and repeated on the biaxial tests, as all the proportional strain tests converge towards a master curve.

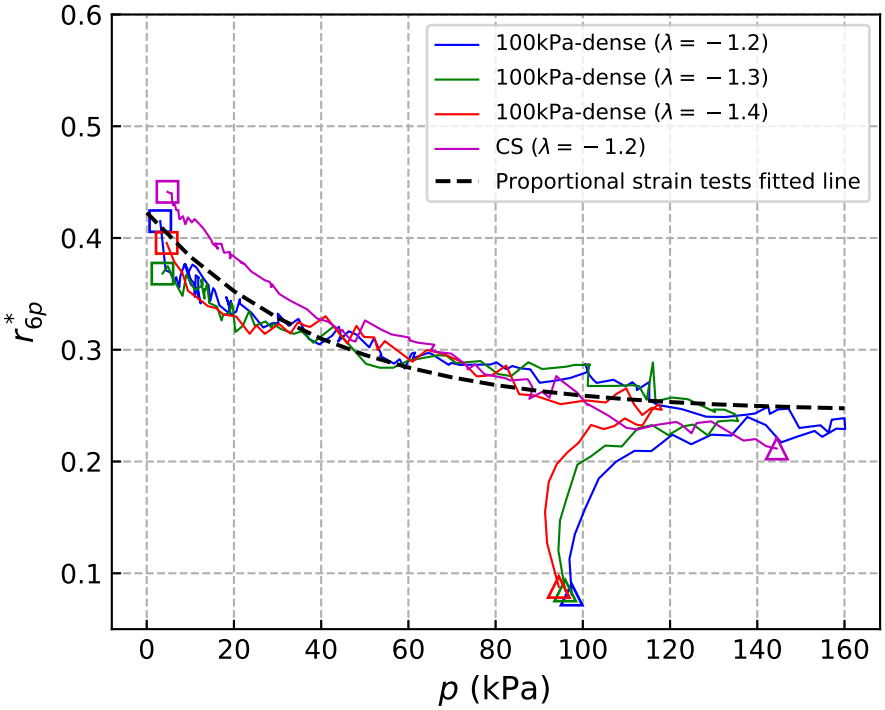

(a)

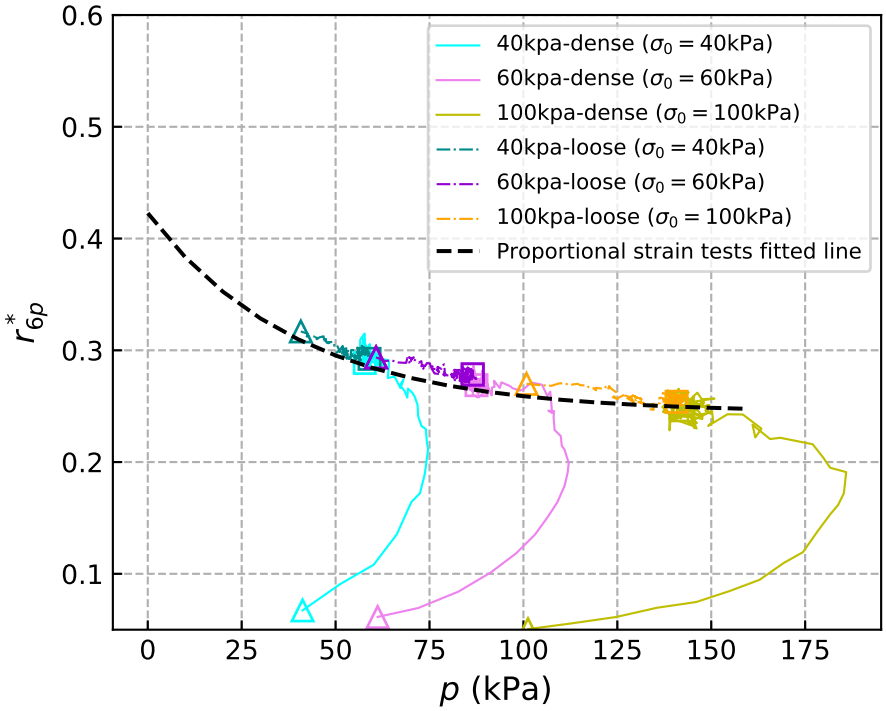

(b)

Figure 13: $p - r^*_{6p}$ for proportional strain (a) and biaxial (b) tests. The start and end points are marked by triangles and squares, respectively. An exponential fit is shown for the dilatant proportional strain tests and repeated on the biaxial tests, as all the proportional strain tests converge towards a master curve.

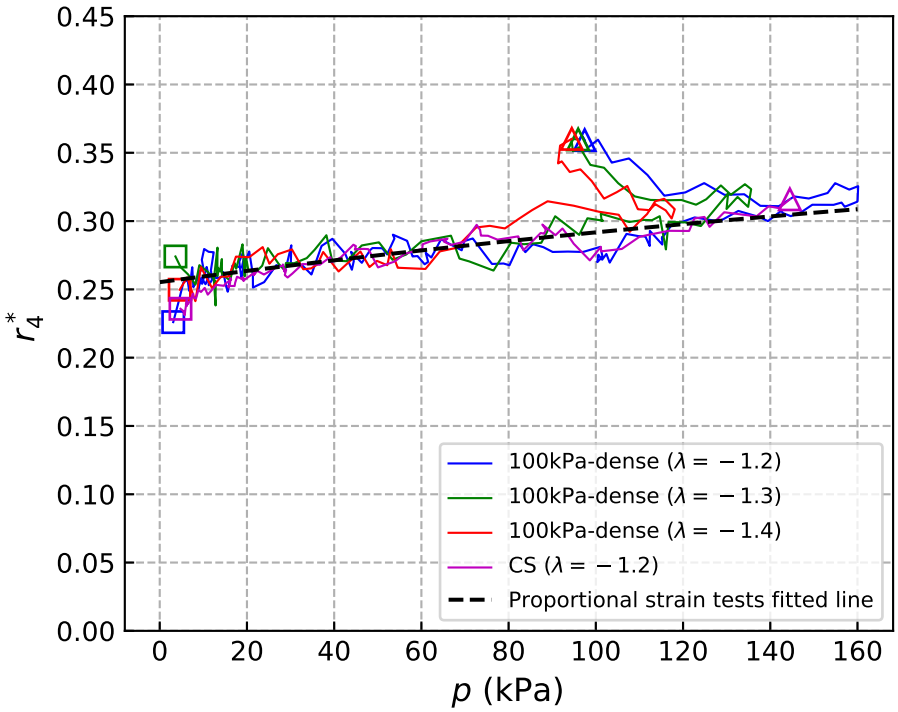

(a)

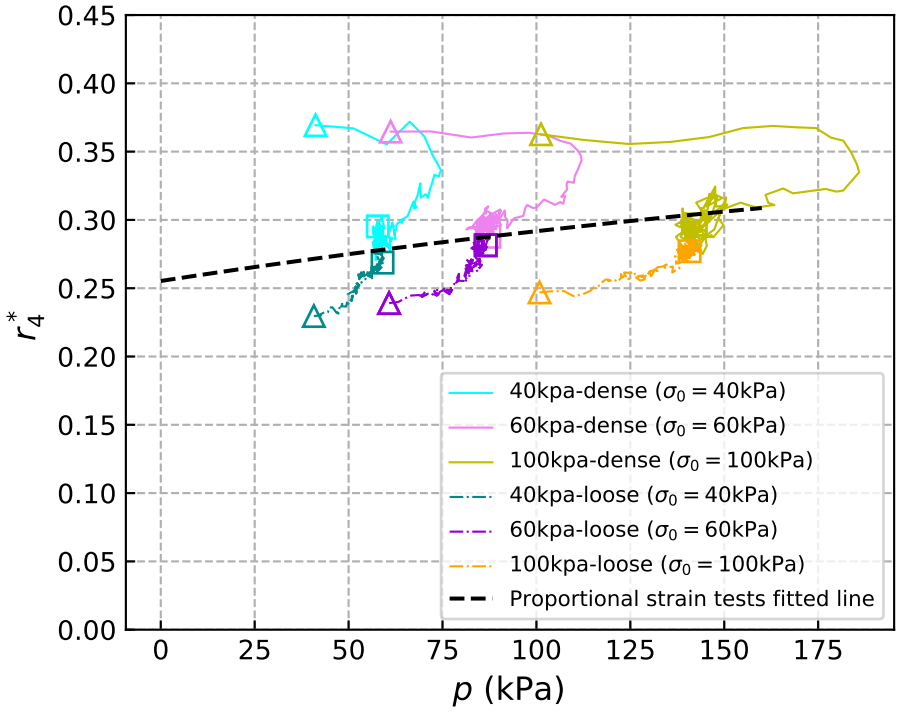

(b)

Figure 14: $p - r_4^*$ for proportional strain (a) and biaxial (b) test. The start and end points are marked by triangles and squares, respectively. An exponential fit is shown for the dilatant proportional strain tests and repeated on the biaxial tests, as the all proportional strain tests converge towards a master curve.

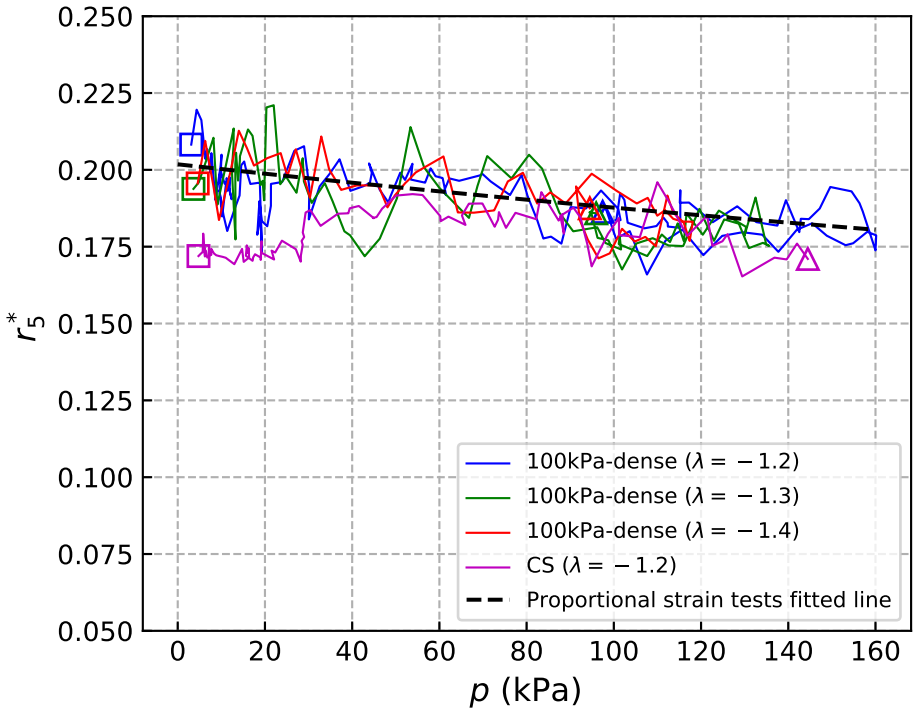

(a)

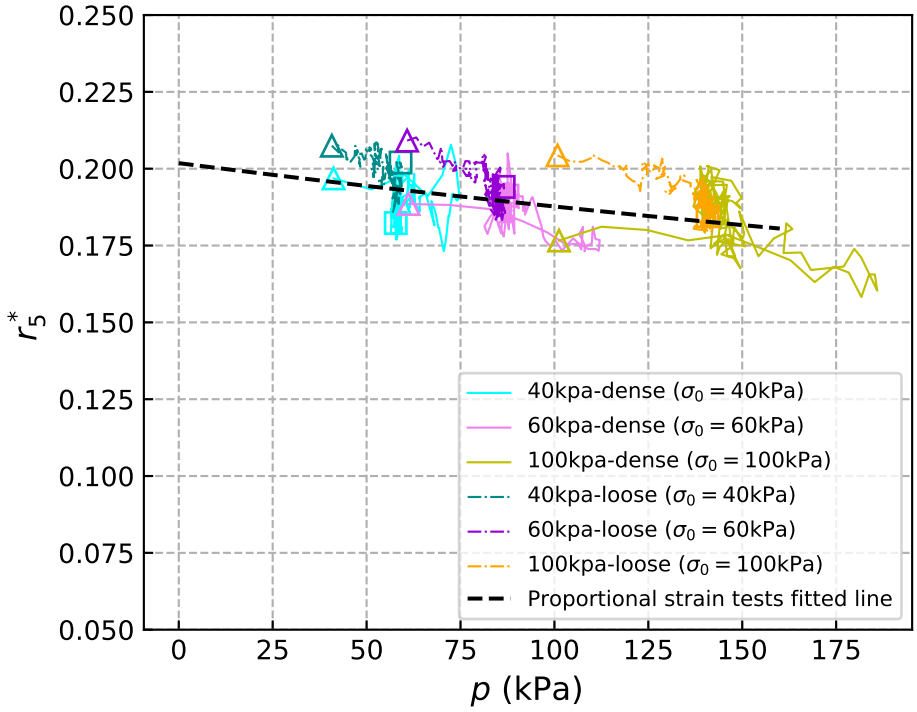

(b)

Figure 15: $p - r_5^*$ for proportional strain (a) and biaxial (b) test. The start and end points are marked by triangles and squares, respectively. An exponential fit is shown for the dilatant proportional strain tests and repeated on the biaxial tests, as all the proportional strain tests converge towards a master curve.

5.2 Meso-loop evolution

To obtain richer information on the critical state, we have analysed meso-loop related indexes in this subsection. As illustrated in Fig.11, meso-loops, enclosed by contact branches, are formed by tessellating the material area [36]. The side number of the loop influences considerably its deformability. In this section, loops will be categorized into four groups according to the side number, referred to as l_i ($i \in [3, 4, 5, 6\text{p}]$), where '6p' refers to a side number equal to or greater than 6. The percentages of categories are given by $r_i = n_i/n_t$, where n_i is the population of the meso-loop with a side number equal to i, and n_t refers to the total population of loops. It is worth noting that the reason for categorizing $r_{6\text{p}}$ is that $r_{7\text{p}}$ (percentage of categories with a side number equal or greater than 7) evolves in a similar way as r_6 [48].The evolution of r_i^* ($i \in [3, 4, 5, 6\text{p}]$) within the shear band for dense specimens and the whole area for loose specimens is tracked along both the dilatant proportional strain loading path and the biaxial loading path.

The results as function of the mean stress p are presented in Fig.12 - 15. Small triangles and squares highlight the start and the end points of the curves and a fitting curve is given based on proportional strain tests in each figure. Two significant characteristics manifest themselves again: (1) the measures of r_i^* ($i \in [3, 4, 5, 6\text{p}]$) from proportional strain tests converge to form a master curve independent of the value of λ; (2) the master curve agrees very well with the critical states characterized by the meso-loop indexes obtained in biaxial tests. These results are in agreement with the premise of ACST.

For the shortest loop l_3, r_3^* continuously decreases from the initial to the ultimate point along all different loading paths. As for the most deformable type of loop l_{6p}, it is in a quite different situation as shown in Fig.13. The value of $r_{6\text{p}}^*$ for the dense samples

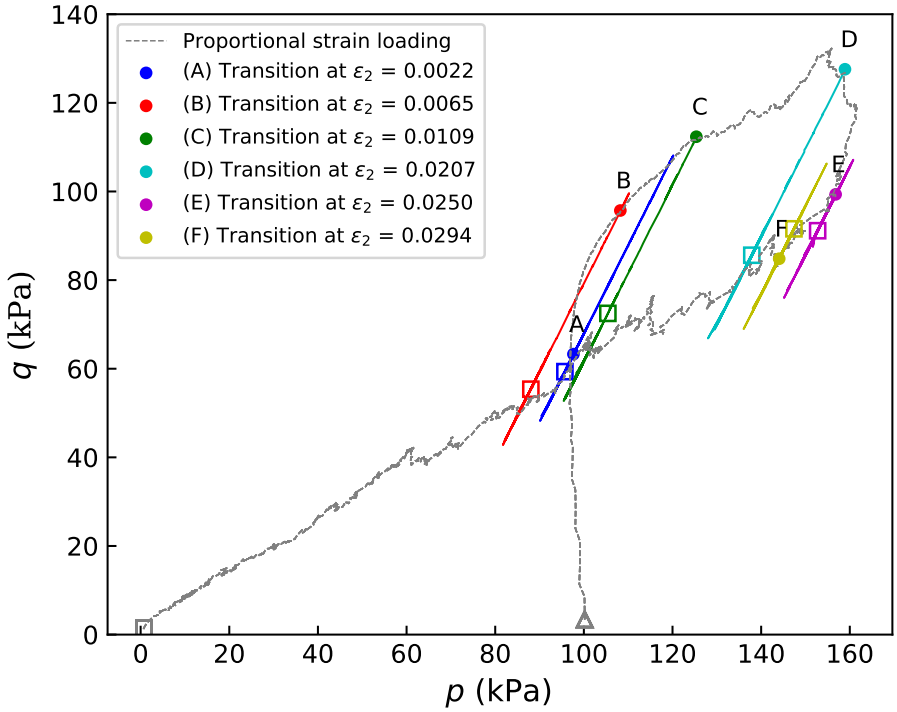

Figure 16: $p-q$ evolution along combining proportional strain and biaxial loading paths. The proportional strain loading with $\lambda = -1.2$ are conducted at first until a certain axial strain level labeled as A, B, C, D, E and F, after that a biaxial loading is performed by keeping the corresponding lateral stress unchanged. The transition states and the average critical states are marked by dots and squares, respectively. The corresponding stress-strain responses are shown in Fig.17

increases during loading, but it decreases for the loose samples.

Different to the fabric tensor based on the statistics of inter-particle contact normals, investigated in Subsection 5.1, that has been widely accepted as a quantitative measure of fabric anisotropy in granular materials [21], the scalar r_i^* is rather a measure characterizing the deformability of granular materials, namely the void ratio. Unlike the fabric anisotropy normalized by the specific volume [21], the evolution of r_i^* depends on p as illustrated in Fig.12 - 15.

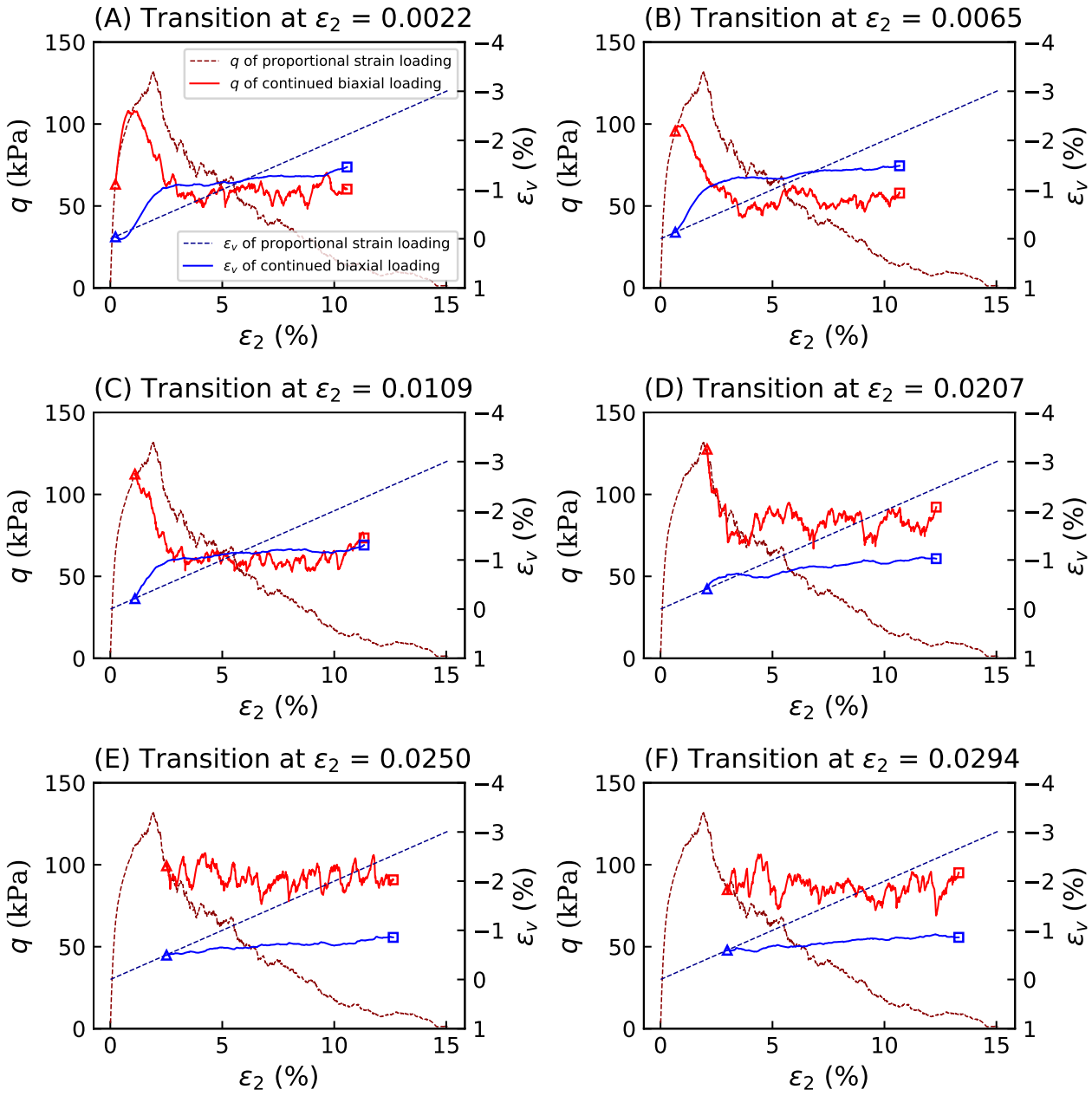

Figure 17: Stress-strain responses along combining proportional strain and biaxial loading paths. The switch states and ultimate states are marked by dots and squares, respectively. The corresponding stress paths are shown in Fig.16

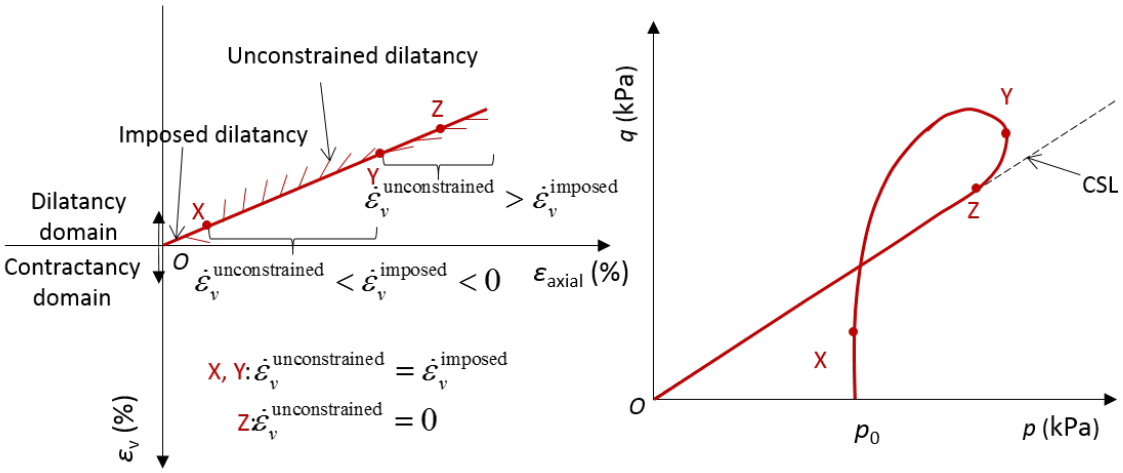

Figure 18: The relation between imposed dilatancy from proportional strain test and unconstrained dilatancy if switched to a biaxial condition according to results in Fig.16 and Fig.17. Note that soil mechanics convention is adopted with positive compression.

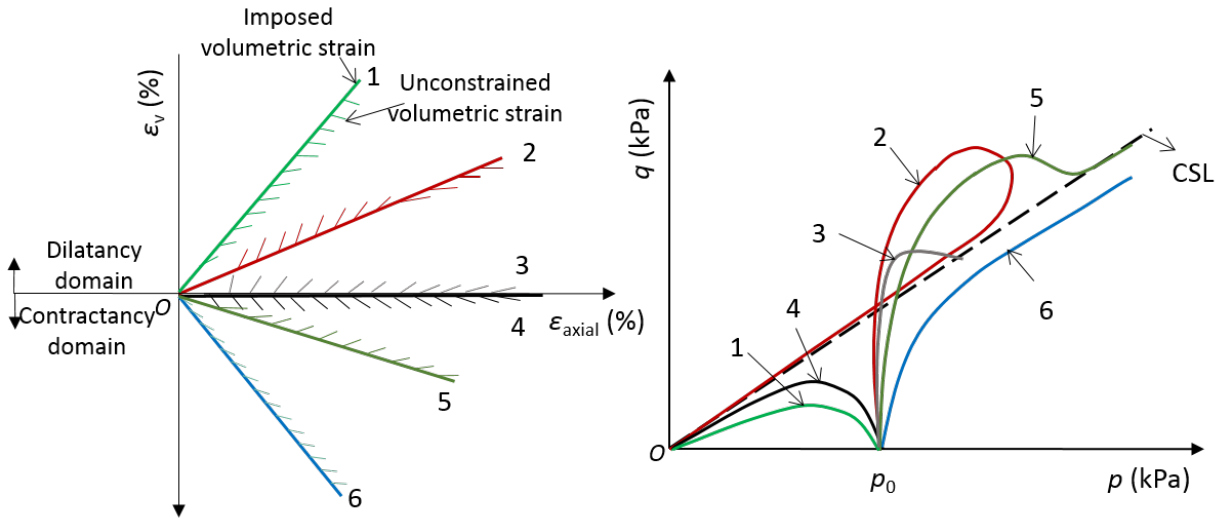

Figure 19: The relation between imposed dilatancy/contractancy in proportional strain tests and unconstrained dilatancy/contractancy expected in biaxial tests in the plane of axial strain vs. volumetric strain (left) and the possible stress paths in the plane of deviatoric stress vs. mean stress (right). The major solid lines represent the imposed dilatancy/contractancy, namely the proportional strain loading paths; the fins denote the incremental unconstrained dilatancy/contractancy if the loading is switched to biaxial conditions.

6 Mixed proportional strain and biaxial loading paths

A complex loading path combining proportional strain and biaxial paths has been simulated to confirm that proportional strain tests can indeed determine the position of critical state in the $e - p - q$ space as shown in Fig.6 and Fig.9. It was conducted as follows: first, the proportional strain path with $\lambda = -1.2$ was imposed; six groups of state data at $\varepsilon_2 = 0.0022$, 0.0065, 0.0109, 0.0250 and 0.0294 were selected; then, a biaxial loading path was performed at each state while the lateral stress was maintained as it was. Such mixed loading paths allow us to assess the existence of critical states according to the definition given in the introduction (continuous shearing with no change in volume or mean pressure, while keeping aligned stress anisotropy with fabric anisotropy). The stress paths along the mixed paths are shown in Fig.16, while the stress and strain responses are presented in Fig.17.

In Fig.16, the six transition states are labelled A, B, C, D, E and F and are marked by zoomed dots. The average critical (p, q) state is marked by squares. It can be observed that all six squares from continued biaxial tests lie along the stress track of proportional strain tests. As seen in Fig.17 , when the loading path was adjusted to a biaxial test at $\varepsilon_2 = 0.0022$, a small compaction, followed by a large dilatancy, appears before a steady regime was reached; when the biaxial test was imposed at $\varepsilon_2 = 0.0065$ or 0.0109, the volume increased at first before it reacheed a steady state; when $\varepsilon_2 = 0.0250$ or 0.0294, the following biaxial loading path fluctuated around constant values for both deviatoric stress and volumetric strain, which means that the switching points correspond to a critical state. The stress-strain evolution of biaxial tests further proves that at relatively large

deformation, the proportional strain loading path will evolve along the critical state line defined in biaxial tests.

Based on the results in Figures 16 and 17, the definition of critical state can be expressed as follows: *for a sample with fixed stress and strain rate directions, a $p-q-e$ state is considered as a critical state if the application of a biaxial loading under the same lateral pressure, starting from this $p-q-e$ state, leads to zero volume strain and zero deviatoric stress evolution.* Note that for such a state, a rotation of the principal stress direction with p and q constant will nevertheless result in a change of e. This result observed for instance in [41] shows that the critical state cannot be described only by the three internal state variables $p-q-e$; additional variables related to the micro-structural anisotropy due to loading direction are necessary to define a state equation for the critical state line [22].

Figures 16 and 17 also provide information for comparing the *unconstrained dilatancy* obtained in biaxial tests with the *imposed dilatancy* in proportional strain tests [ii]. As illustrated in Fig.18, the solid line represents the imposed dilatancy with respect to axial strain. The fixed dilatant rate is characterized by the slope of the line. The fins give the unconstrained dilatancy rate (namely a direction of incremental volumetric strain), that would be observed if the loading were switched to a biaxial one. At the beginning, the imposed dilatancy is larger than the unconstrained dilatancy (from point O to X), the mean stress p decreases slightly from p_0 to X. When the imposed dilatancy is smaller than the unconstrained dilatancy expressed as $\dot{\varepsilon}_v^{\text{unconstrained}} < \dot{\varepsilon}_v^{\text{imposed}} < 0$ (from point X to Y), the stress response p increases from X to Y. The unconstrained dilatancy decreases contin-

[ii]Note that the terms *unconstrained* and *imposed* are used to recall that the volumetric strain is a response variable in a biaxial loading while it is a control variable in proportional strain tests.

uously thanks to the imposed dilatancy. The states at $\varepsilon_2 = 0.0065$ and 0.0109 in Fig.17 belong to this domain. At points X and Y, where the unconstrained dilatancy equals the imposed dilatancy, the mean stress p reaches the peak. The state at $\varepsilon_2 = 0.0207$ in the proportional strain test is close to point Y. After point Y, the unconstrained dilatancy decreases continuously to become smaller than the imposed dilatancy, described as $0 > \dot{\varepsilon}_v^{\text{unconstrained}} > \dot{\varepsilon}_v^{\text{imposed}}$ till zero unconstrained dilatancy at point Z ($\dot{\varepsilon}_v^{\text{unconstrained}} = 0$). At point Z, the stress path reaches the CSL defined by biaxial tests. If a biaxial path is followed after point Z, $\dot{\varepsilon}_v^{\text{unconstrained}} = 0$ occurs as shown in the results from mixed tests switched at $\varepsilon_2 = 0.0250$ and 0.0294. The further imposed dilatancy after point Y leads the stress path to turn back to approach point O along the CSL. In conclusion, when the imposed dilatancy is smaller (larger) than the unconstrained dilatancy, the mean stress p increases (decreases).

The results in Fig.7 suggest that the relation between imposed dilatancy/contractancy in proportional strain tests and dilatancy/contractancy expected in biaxial tests can be categorized as shown in Fig.19. The strain path 1 represents a situation for which the imposed dilatancy is larger than the unconstrained dilatancy (contractancy can be regarded as the negative dilatancy) from the beginning. This strain path leads to a liquefaction presented as stress path 1. Dilatant proportional strain loading path 2 leads to a more complex response, as discussed before.

The proportional strain test with zero volume change (often referred to as undrained test) can be categorized as one of two types, depending on whether $\dot{\varepsilon}_v^{\text{unconstrained}} < 0$ at the beginning (path 3) or $\dot{\varepsilon}_v^{\text{unconstrained}} > 0$ (path 4). The unconstrained dilatancy along loading path 3 tends toward zero (horizontal direction), when approaching the critical

state. Conversely, loading path 4, representing an isochoric test on a loose sample, results in liquefaction.

As for the contracting proportional strain path, two groups can be identified according to whether the stress path crosses the CSL as paths 5 and 6 do. At the beginning of curve 5, the unconstrained contractancy being larger than the imposed contractancy, the mean stress p decreases slightly. Shortly afterwards, the unconstrained contractancy becomes smaller than the imposed contractancy, which leads to the increase in p. The direction of the fins tending to become horizontal is synchronized with the $p - q$ curve approaching the CSL when strain localization takes place within the sample. The representation of curve 5 is based on results from simulations of mixed biaxial/contracting proportional strain loading paths (these results are not presented in this paper whose focus is upon dilatant proportional strain loading paths). Curve 6 represents the situation where the unconstrained contractancy is always smaller than the imposed contractancy, which leads to a continuous increase in p.

To summarize, the mean stress will increase in the dilatancy domain, when the imposed dilatancy rate is smaller than the unconstrained dilatancy rate. When the imposed dilatancy is larger than the unconstrained dilatancy, the mean stress decreases and tends to 0 for large volumetric strain. When the imposed dilatancy is first smaller and then larger than the unconstrained dilatancy, the stress path is likely to undergo a stress loop. In the contractancy domain, when the imposed contractancy is larger than the unconstrained contractancy, the mean stress increases. On the other hand, an imposed contractancy being smaller than the unconstrained contractancy will result in a decrease in p.

These numerical findings can also be interpreted in terms of dilatancy angles if we recall that the dilatancy angle is defined in 2D by $\sin\psi = \dot{\varepsilon}_v/\dot{\varepsilon}_{\mathrm{d}} = \dot{\varepsilon}_v/(2\dot{\varepsilon}_{\mathrm{axial}} - \dot{\varepsilon}_v)$. As long as it can be assumed that granular materials follow a standard non-associated elasto-plastic behavior (which is true in 2D or axisymmetric conditions for instance[28]), the dilatancy angle characterize the flow rule, and the unconstrained dilatancy can be viewed as a material property. This broadens the scope of the analysis summarized in Figure 19 insofar, as making it independent of the loading paths considered (at least for 2D or axisymmetric conditions). The present results are also consistent with previous experimental and theoretical studies [8, 9]. In [8], the dilatancy rate defined by $\dot{\varepsilon}_v/\dot{\varepsilon}_{\mathrm{axial}}$ can be related to the effective mean pressure. In the criterion of liquefaction given in [9], the dilatancy angle obtained from the flow rule and the mean pressure at a given initial void ratio have a non-linear negative correlation.

7 Conclusion and outlook

By simulating proportional strain tests, biaxial tests and complex loading paths combining biaxial and proportional strain paths using DEM, we have explored through a series of mechanical and fabric indexes the relation between proportional strain tests and critical states from biaxial tests.

In considering the results obtained from biaxial tests, we have observed that all structural variables (e^*, α_c^*, r_i^*) within shear bands for specimens experiencing a localized kinematic pattern will converge to the same values as for specimens experiencing a diffuse kinematic pattern at critical state along the same biaxial loading path. These results

are consistent with the conclusion drawn by Zhu et al. [48] that localization and diffuse patterns share the same fabric properties.

As for proportional strain tests, when the dilatant rate is relatively small and the axial strain is large enough, a stress path in the $p-q$ plane will finally reach the critical state line defined by biaxial tests after experiencing a stress loop. The curves on the $p-e^*$ (void ratio), $p-\alpha_c^*$ (fabric anisotropy intensity defined from contact normal direction) and $p-r_i^*$ (population of meso-loops) planes also converge towards a master curve regardless of the magnitude of dilatancy characterized by $\lambda = -1.2, -1.3, -1.4$. In combining these results, it can be inferred that any dilatant volume change will always result in similar (p, q, e^*, α_c^*, r_i^*) states after the material memory has been erased.

More interestingly is the relation observed between the mechanical states reached along a proportional strain test and the critical states obtained from biaxial tests within the framework of ACST. Macroscopic responses (p, q, e^*) and fabric-related measures (α_c^*, r_i^*) in homogeneous domains along biaxial tests evolve towards the evolution curve of those variables from proportional strain tests at critical state. Given these results, only one single test is therefore necessary to construct the classical critical state line in (p - q - e^* - α_c^* - r_i^*) space for any granular material. Therefore, the CS concept can be generalized to a wide class of loading paths which shows that CS acts as a general attractor irrespective of the loading path considered. This idea of proportional strain paths enriched considerably the data base for confirmation of CST and ACST.

The mixed proportional strain and biaxial loading paths also confirm this relation. A more general definition of CS can be given as follows: a $p-q-e$ state, for a sample with

constant stress and strain rate directions, after a given loading history, is considered at critical state if the application of a biaxial loading under the same lateral pressure starting from this $p-q-e$ state leads to zero volume strain and zero deviatoric stress evolution.

In addition, the comparison between the imposed dilatancy/contractancy along proportional strain paths and unconstrained dilatancy/contractancy expected along biaxial paths provides valuable information to the interpretation of the various loading paths obtained in $p-q$ plane for proportional strain loading paths. Along proportional strain tests, the volumetric strain, which tends to be steady, produces the stress path approaching the CSL.

Proportional strain loading paths are attracted by the critical state line. For samples initially at critical state (after a biaxial loading for instance), a proportional strain loading imposes the evolution of the sample state along the critical state line. Even for samples not initially at critical state, when subjected to proportional strain loading, the micro-structure rearranges itself and reaches geometrical arrangements corresponding to critical state. This memory fading is probably a key ingredient affecting complex systems and may also be at the origin of emerging properties. It will be of great interest to further investigate the underpinning mechanisms of memory fading according to the kinematic pattern (localization vs. diffuse mode). In addition, from a microscopic point of view, critical state is a dynamic equilibrium, where only statistics are constant. Most constitutive models for granular materials describe the critical state from a phenomenological point of view ignoring the micro-mechanical dynamics. Allowing critical state to emerge in micro-mechanical constitutive models from a physical viewpoint will provide a challenging topic for the future. One limitation of this study is that all conclusions above are

drawn based on 2D simulations. The extension to 3D, numerically and experimentally, will be attempted in the future.

Acknowledgement

The authors wish to thank Professor Félix Darve (3SR) for insightful discussions and his valuable comments and suggestions on how to improve this work. The authors also thank Dr. Jiaying Liu (Wuhan University) for her valuable comments. The authors express their sincere thanks to the French Research Network GeoMech (GDRI CNRS) for promoting positive and convivial interactions among researchers. The support from China Scholarship Council (CSC) under the Grant CSC Number 201801810030 and from the BRGM (French geological Survey) under the contract RP19DRP023 is gratefully acknowledged. The constructive comments by the reviewers are highly appreciated.

References

[1] K. Been and M. G. Jefferies. A state parameter for sands. *Géotechnique*, 35(2):99–112, 1985.

[2] K. Been, M. G. Jefferies, and J. Hachey. Critical state of sands. *Géotechnique*, 41(3):365–381, 1991.

[3] A. Casagrande. Characteristics of cohesionless soils affecting the stability of slopes and earth fills. *Journal of the Boston Society of Civil Engineers*, 23(1):13–32, 1936.

[4] J. Chu, S. C. Lo, and I. K. Lee. Strain-softening behavior of granular soil in strain-path testing. *Journal of Geotechnical Engineering*, 118(2):191–208, 1992.

[5] P. A. Cundall and O. D. Strack. A discrete numerical model for granular assemblies. *Géotechnique*, 29(1):47–65, 1979.

[6] F. Da Cruz, S. Emam, M. Prochnow, J.-N. Roux, and F. Chevoir. Rheophysics of dense granular materials: Discrete simulation of plane shear flows. *Physical Review E*, 72(2):021309, 2005.

[7] A. Daouadji, P.-Y. Hicher, M. Jrad, B. Sukumaran, and S. Belouettar. Experimental and numerical investigation of diffuse instability in granular materials using a microstructural model under various loading paths. *Géotechnique*, 63(5):368–381, 2013.

[8] A. Daouadji, M. Jrad, G. Robin, A. Brara, and E. M. Daya. Phase transformation states of loose and dense granular materials under proportional strain loading. *Journal of Engineering Mechanics*, 143(1):C4016007, 2017.

[9] F. Darve. Liquefaction phenomenon of granular materials and constitutive stability. *Engineering Computations: Int J for Computer-Aided Engineering*, 13(7):5–28, 1996.

[10] J. Desrues, R. Chambon, M. Mokni, and F. Mazerolle. Void ratio evolution inside shear bands in triaxial sand specimens studied by computed tomography. *Géotechnique*, 46(3):529–546, 1996.

[11] A. Drescher and G. D. J. De Jong. Photoelastic verification of a mechanical model for the flow of a granular material. *Journal of the Mechanics and Physics of Solids*, 20(5):337–340, 1972.

[12] P. Fu and Y. F. Dafalias. Fabric evolution within shear bands of granular materials and its relation to critical state theory. *International Journal for Numerical and Analytical Methods in Geomechanics*, 35(18):1918–1948, 2011.

[13] P. Fu and Y. F. Dafalias. Relationship between void- and contact normal- based fabric tensors for 2d idealized granular materials. *International Journal of Solids and Structures*, 63:68–81, 2015.

[14] Z. Gao, J. Zhao, X. S. Li, and Y. F. Dafalias. A critical state sand plasticity model accounting for fabric evolution. *International Journal for Numerical and Analytical Methods in Geomechanics*, 38(4):370–390, 2014.

[15] E. Ibraim, J. Lanier, D. Muir Wood, and G. Viggiani. Strain path controlled shear tests on an analogue granular material. *Géotechnique*, 60(7):545–559, 2010.

[16] R. Kawamoto, E. Andò, G. Viggiani, and J. E. Andrade. All you need is shape: Predicting shear banding in sand with ls-dem. *Journal of the Mechanics and Physics of Solids*, 111:375–392, 2018.

[17] N. P. Kruyt and L. Rothenburg. On micromechanical characteristics of the critical state of two-dimensional granular materials. *Acta Mechanica*, 225(8):2301–2318, 2014.

[18] N. P. Kruyt and L. Rothenburg. A micromechanical study of dilatancy of granular materials. *Journal of the Mechanics and Physics of Solids*, 95:411–427, 2016.

[19] X. Li and X. S. Li. Micro-macro quantification of the internal structure of granular materials. *Journal of Engineering Mechanics*, 135(7):641–656, 2009.

673 [20] X. S. Li. Modeling of dilative shear failure. *Journal of Geotechnical and Geoenvi-*
674 *ronmental Engineering*, 123(7):609–616, 1997.

675 [21] X. S. Li and Y. Dafalias. Dissipation consistent fabric tensor definition from DEM
676 to continuum for granular media. *Journal of the Mechanics and Physics of Solids*,
677 78:141–153, 2015.

678 [22] X. S. Li and Y. F. Dafalias. Anisotropic critical state theory: role of fabric. *Journal*
679 *of Engineering Mechanics*, 138(3):263–275, 2012.

680 [23] X. S. Li, Y. F. Dafalias, and Z. L. Wang. State dependant dilatancy in critical-state
681 constitutive modelling of sand. *Canadian Geotechnical Journal*, 36(4):599–611, 1999.

682 [24] J. Liu, F. Nicot, and W. Zhou. Sustainability of internal structures during shear
683 band forming in 2d granular materials. *Powder Technology*, 338:458–470, 2018.

684 [25] J. Liu, A. Wautier, S. Bonelli, F. Nicot, and F. Darve. Macroscopic softening in
685 granular materials from a mesoscale perspective. *International Journal of Solids and*
686 *Structures*, 2020.

687 [26] J. Liu, W. Zhou, G. Ma, S. Yang, and X. Chang. Strong contacts, connectivity and
688 fabric anisotropy in granular materials: A 3d perspective. *Powder Technology*, 2020.

689 [27] F. Nicot, A. Daouadji, N. Hadda, M. Jrad, and F. Darve. Granular media failure
690 along triaxial proportional strain paths. *European Journal of Environmental and*
691 *Civil Engineering*, 17(9):777–790, 2013.

692 [28] F. Nicot and F. Darve. Basic features of plastic strains: from micro-mechanics to
693 incrementally nonlinear models. *International Journal of Plasticity*, 23(9):1555–1588,
694 2007.

[29] F. Nicot and F. Darve. Diffuse and localized failure modes: two competing mechanisms. *International Journal for Numerical and Analytical Methods in Geomechanics*, 35(5):586–601, 2011.

[30] F. Nicot and F. Darve. The H microdirectional model: accounting for a mesoscopic scale. *Mechanics of Materials*, 43(12):918–929, 2011.

[31] F. Nicot, N. Hadda, M. Guessasma, J. Fortin, and O. Millet. On the definition of the stress tensor in granular media. *International Journal of Solids and Structures*, 50(14-15):2508–2517, 2013.

[32] F. Nicot, L. Sibille, and P.-Y. Hicher. Micro–macro analysis of granular material behavior along proportional strain paths. *Continuum Mechanics and Thermodynamics*, 27(1-2):173–193, 2015.

[33] C. O'Sullivan, J. D. Bray, and S. Li. A new approach for calculating strain for particulate media. *International Journal for Numerical and Analytical Methods in Geomechanics*, 27(10):859–877, 2003.

[34] K. Roscoe, A. Schofield, and C. Wroth. On the yielding of soils. *Géotechnique*, 8(1):22–53, 1958.

[35] E. Salvatore, G. Modoni, E. Andò, M. Albano, and G. Viggiani. Determination of the critical state of granular materials with triaxial tests. *Soils and Foundations*, 57(5):733–744, 2017.

[36] M. Satake. A discrete-mechanical approach to granular materials. *International journal of engineering science*, 30(10):1525–1533, 1992.

[37] A. Schofield and P. Wroth. *Critical State Soil Mechanics*, volume 310. McGraw-Hill London, 1968.

[38] J. Shi and P. Guo. Induced fabric anisotropy of granular materials in biaxial tests along imposed strain paths. *Soils and Foundations*, 58(2):249–263, 2018.

[39] L. Sibille, N. Hadda, F. Nicot, A. Tordesillas, and F. Darve. Granular plasticity, a contribution from discrete mechanics. *Journal of the Mechanics and Physics of Solids*, 75:119–139, 2015.

[40] V. Smilauer, E. Catalano, B. Chareyre, S. Dorofeenko, J. Duriez, N. Dyck, J. Elias, B. Er, A. Eulitz, A. Gladky, et al. Yade documentation 2nd ed., 2015.

[41] A. I. Theocharis, E. Vairaktaris, Y. F. Dafalias, and A. G. Papadimitriou. Necessary and sufficient conditions for reaching and maintaining critical state. *International Journal for Numerical and Analytical Methods in Geomechanics*, 43(12):2041–2055, 2019.

[42] R. Verdugo and K. Ishihara. The steady state of sandy soils. *Soils and Foundations*, 36(2):81–91, 1996.

[43] R. Wan, F. Nicot, and F. Darve. *Failure in Geomaterials: a Contemporary Treatise*. Elsevier, 2017.

[44] R. G. Wan and P. J. Guo. Stress dilatancy and fabric dependencies on sand behavior. *Journal of Engineering Mechanics*, 130(6):635–645, 2004.

[45] A. Wautier, S. Bonelli, and F. Nicot. Dem investigations of internal erosion: Grain transport in the light of micromechanics. *International Journal for Numerical and Analytical Methods in Geomechanics*, 43(1):339–352, 2019.

[46] Z.-Y. Yin and C. S. Chang. Stress–dilatancy behavior for sand under loading and unloading conditions. *International Journal for Numerical and Analytical Methods in Geomechanics*, 37(8):855–870, 2013.

[47] J. Zhao and N. Guo. Unique critical state characteristics in granular media considering fabric anisotropy. *Géotechnique*, 63(8):695, 2013.

[48] H. Zhu, H. N. Nguyen, F. Nicot, and F. Darve. On a common critical state in localized and diffuse failure modes. *Journal of the Mechanics and Physics of Solids*, 95:112–131, 2016.